The Astrophysical Journal, 999:176 (27pp), 2026 March 10 https://doi.org/10.3847/1538-4357/ae374c

SN 2021aaev: A Hydrogen-rich Superluminous Supernova with Early Flash and Long-lived Circumstellar Interaction in an Unusual Host Environment

Yang Hu (胡 阳)[1], Ragnhild Lunnan[1], Priscila J. Pessi[1,2], Alberto Saldana-Lopez[1], Anders Jerkstrand[1], Jesper Sollerman[1], Steve Schulze[3], Joseph P. Anderson[4], Seán J. Brennan[1,5], Stefano P. Cosentino[6], Anjasha Gangopadhyay[1], Anamaria Gkini[1], Mariusz Gromadzki[7], Matthew J. Hayes[1], Cosimo Inserra[8], Tomás E. Müller-Bravo[9,10], Matt Nicholl[11], Giuliano Pignata[12], Avinash Singh[1], Jacob L. Wise[13], Lin Yan[14], Judy Adler[15], Ting-Wan Chen[16], Tracy X. Chen[15], Mansi M. Kasliwal[17], Thallis Pessi[4], Irene Salmaso[18,19], and David R. Young[11]

[1] The Oskar Klein Centre, Department of Astronomy, Stockholm University, AlbaNova, SE-10691 Stockholm, Sweden
[2] Astrophysics Division, National Centre for Nuclear Research, Pasteura 7, 02-093 Warsaw, Poland
[3] Center for Interdisciplinary Exploration and Research in Astrophysics (CIERA), Northwestern University, 1800 Sherman Ave, Evanston, IL 60201, USA
[4] European Southern Observatory, Alonso de Córdova 3107, Casilla 19, Santiago, Chile
[5] Max-Planck-Institut für extraterrestrische Physik, Giessenbachstrasse 1, 85748 Garching, Germany
[6] Department of Physics and Astronomy, "E. Majorana," University of Catania, Italy
[7] Astronomical Observatory, University of Warsaw, Al. Ujazdowskie 4, 00-478 Warszawa, Poland
[8] Cardiff Hub for Astrophysics Research and Technology, School of Physics & Astronomy, Cardiff University, Queens Buildings, The Parade, Cardiff, CF24 3AA, UK
[9] School of Physics, Trinity College Dublin, The University of Dublin, Dublin 2, Ireland
[10] Instituto de Ciencias Exactas y Naturales (ICEN), Universidad Arturo Prat, Chile
[11] Astrophysics Research Centre, School of Mathematics and Physics, Queens University Belfast, Belfast, BT7 1NN, UK
[12] Instituto de Alta Investigación, Universidad de Tarapacá, Casilla 7D, Arica, Chile
[13] Astrophysics Research Institute, Liverpool John Moores University, 146 Brownlow Hill, Liverpool, L3 5RF, UK
[14] Caltech Optical Observatories, California Institute of Technology, Pasadena, CA 91125, USA
[15] IPAC, California Institute of Technology, 1200 E. California Blvd, Pasadena, CA 91125, USA
[16] Graduate Institute of Astronomy, National Central University, 300 Jhongda Road, 32001, Jhongli, Taiwan
[17] California Institute of Technology, 1200 E. California Boulevard, Pasadena, CA 91125, USA
[18] INAF-Osservatorio Astronomico di Capodimonte, Salita Moiariello 16, 80131 Napoli, Italy
[19] INAF-Osservatorio Astronomico di Padova, Vicolo dell'Osservatorio 5, 35122 Padova, Italy
Received 2025 August 15; revised 2025 December 28; accepted 2026 January 7; published 2026 March 2

Abstract

We present photometric and spectroscopic observations of SN 2021aaev, a hydrogen-rich, superluminous supernova with persistent (at least ∼100 days) narrow Balmer lines (SLSN-IIn) at redshift $z = 0.1557$. SN 2021aaev rose over 28.1 ± 1.0 rest-frame days after explosion, reaching a peak absolute magnitude of -21.46 ± 0.01 in the ATLAS *o* band. The prepeak spectra resemble those of typical Type IIn SNe with flash-ionization features arising from the interaction with a dense, confined circumstellar medium (CSM), albeit the flash timescale is longer than usual (>20 days). Postpeak, the narrow emission lines evolve slowly, and the absence of ejecta features indicates strong deceleration by the CSM. The total radiated energy (about 1.41×10^{51} erg) is possibly explained by a low-mass (1–2 $M_\odot$) ejecta ploughing into a massive (9–19 $M_\odot$), extended (outer radius $>1 \times 10^{16}$ cm) H-rich CSM, or alternatively by magnetar-powered models. Interestingly, the host environment consists of a spiral galaxy with a red substructure in the southeastern part, and the SN's exact location coincides with this quiescent red region (star formation rate $= 0.02^{+0.13}_{-0.02}\, M_\odot\, \mathrm{yr}^{-1}$). Given the atypical environment and the obscuring effect of the massive CSM, a thermonuclear (Type Ia-CSM) origin cannot be ruled out. Altogether, SN 2021aaev is a compelling case to study the diversity of SLSN-IIn features and their host environments.

Unified Astronomy Thesaurus concepts: Type II supernovae (1731); Core-collapse supernovae (304); Supernovae (1668); Stellar mass loss (1613); Circumstellar matter (241); Massive stars (732)

Materials only available in the online version of record: machine-readable tables

1. Introduction

Superluminous supernovae (SLSNe) are a rare class of extremely luminous stellar explosions, with peak luminosities typically exceeding what can be explained in the framework of ordinary core-collapse supernovae (CCSNe). The exact definition of this class often involves a peak luminosity threshold. Historically, this threshold has been chosen somewhat arbitrarily based on a nominal value, e.g., −21 mag in the optical (A. Gal-Yam 2012) or −20 mag in the optical (D. A. Perley et al. 2016), that can separate SLSNe from ordinarily bright SNe. This threshold has evolved over time, with proposed values varying across different subclasses of SLSNe (see, e.g., A. Gal-Yam 2019; T. Kangas et al. 2022; P. J. Pessi et al. 2025b).

SLSNe are broadly divided into Type I superluminous supernovae (SLSNe-I; hydrogen-poor SLSNe) and Type II superluminous supernovae (SLSNe-II; hydrogen-rich SLSNe),

based on the absence or presence of hydrogen in their spectra. With a growing number of observations, most SLSNe-I have been found to exhibit a series of distinctive O II features spanning 3500−5000 Å in their early spectra (R. M. Quimby et al. 2011, 2018; P. A. Mazzali et al. 2016; A. Gal-Yam 2019) with a few exceptions (see, e.g., C. P. Gutiérrez et al. 2022; S. Schulze et al. 2024). However, for SLSNe-II, no ubiquitous spectroscopic property has been identified. The majority exhibit narrow H lines and can be further classified as SLSNe-IIn (or simply SNe IIn; T. Kangas et al. 2022), while a smaller subset exhibit broad Balmer emission in their early photospheric phase (see, e.g., S. Gezari et al. 2009; C. Inserra et al. 2018; T. Kangas et al. 2022). Some works advocate a more restrictive definition that requires the presence of broad Hα emission (FWHM $\geqslant$ 5000 km s^{-1}) in early photospheric phase for classification as a SLSN-II (e.g., C. Inserra et al. 2018; T. Kangas et al. 2022). However, early-time spectroscopy is not always available, making it difficult to apply such a criterion consistently. In this work, we refer to all H-rich SNe with peak luminosities brighter than −20 mag as SLSNe-II (see, e.g., P. J. Pessi et al. 2025b), and refer to those with narrow H lines in the early photospheric phase as the subclass SLSNe-IIn.

SLSNe-II are rare. Early studies estimated their occurrence rate to be approximately 0.1% of all CCSNe (R. M. Quimby et al. 2013; M. Taylor et al. 2014). Nevertheless, several individual SLSNe-II have been investigated, e.g., SN 2006gy (E. O. Ofek et al. 2007; N. Smith et al. 2007),[20] SN 2008am (E. Chatzopoulos et al. 2011), SN 2008es (S. Gezari et al. 2009; A. A. Miller et al. 2009), SN 2010jl (R. Stoll et al. 2011; C. Fransson et al. 2014), SN 2016aps (A. Suzuki et al. 2021), SN 2017hcc (S. Moran et al. 2023), and SN 2021adxl (S. J. Brennan et al. 2024), along with analyses of small samples (e.g., C. Inserra et al. 2018). Recently, T. Kangas et al. (2022) and P. J. Pessi et al. (2025b) presented studies on the light curves of SLSNe-II from the Zwicky Transient Facility (ZTF) survey (E. C. Bellm et al. 2019; M. J. Graham et al. 2019; F. J. Masci et al. 2019; R. Dekany et al. 2020). T. Kangas et al. (2022) analyzed 14 SLSNe-II with broad Balmer emission in the ZTF sample, and P. J. Pessi et al. (2025b) analyzed the remaining 107 events exceeding the −20 mag threshold, together constituting the largest SLSN-II light-curve sample to date. These studies show that SLSNe-II have heterogeneous light-curve properties. They are also energetic events, with peak bolometric luminosities typically in the range of 10^{43}−10^{44} erg s^{-1}, and total radiated energies exceeding 10^{51} erg. In extreme cases, the total energy may exceed what can be explained by the core-collapse neutrino-driven explosion mechanism (see, e.g., H.-T. Janka 2012; G. Terreran et al. 2017).

Spectroscopically, the majority of SLSNe-II are SLSNe-IIn, and the narrow H lines originate from the photoionized, H-rich, slow-moving circumstellar medium (CSM; N. N. Chugai 1997). When the SN ejecta collide with this CSM, they generate shock waves that convert ejecta kinetic energy into radiation and power the extraordinarily luminous light curves (R. A. Chevalier & C. Fransson 1994). Additional spectroscopic evidence for CSM interaction is the presence of highly ionized narrow lines (e.g., He II λ4686). These so-called flash-ionization features typically appear within hours to days after explosion, when the ejecta encounters dense and confined CSM, and disappear before peak luminosity (transients exhibiting these features are thus dubbed "flashers"; A. Gal-Yam et al. 2014; D. Khazov et al. 2016; R. J. Bruch et al. 2023). Capturing flash features requires early-time spectroscopy, which remains rare for SLSNe-IIn because surveys (e.g., ZTF) preferentially select SLSN candidates with long rise times to reduce non-SLSN contamination (T. Kangas et al. 2022; Z. H. Chen et al. 2023a).

CSM interaction is a promising mechanism for explaining both the high peak luminosities and the observed spectral features of SLSNe-IIn. While we directly observe the radiation from CSM interaction, the nature of the progenitor itself is largely obscured by it. In some cases, such as SN 2006gy, a thermonuclear explosion inside a massive common envelope has been proposed (e.g., A. Jerkstrand et al. 2020), suggesting that other explosion mechanisms may underlie transients that we perceive as SLSNe-IIn. Meanwhile, the origin of the CSM from the progenitor's mass loss remains an open question, with several viable processes proposed, including stellar winds (L. B. Lucy & P. M. Solomon 1970; J. Puls et al. 2008), eruptive mass loss (A. Heger et al. 2003; S. E. Woosley et al. 2007; N. Smith & W. D. Arnett 2014; S. E. Woosley 2017), or mass transfer in binary or multiple systems (J. Petrovic et al. 2005; Y. Götberg et al. 2017; S.-C. Yoon et al. 2017; E. Laplace et al. 2020).

Notably, past studies have already widely used CSM interaction to explain the powering of normal Type IIn supernovae (SNe IIn; E. M. Schlegel 1990), where the brighter end of the population can reach a peak luminosity <-19 mag (A. Nyholm et al. 2020). The potential overlap with the nominal −20 mag threshold has led to questions on the validity of using a magnitude cutoff for classification (see, e.g., D. Hiramatsu et al. 2024). This also raises the broader issue of whether SLSNe-IIn represent a distinct population or simply the brighter extension of the same physical mechanisms, and what CSM properties might drive the diversity in observed luminosities among H-rich interacting SNe.

In addition to CSM interaction, several other powering mechanisms have been proposed to explain the light curves of SLSNe, but with less observed spectroscopic evidence. While initially suggested for SLSNe-I, these mechanisms can also be applied to SLSNe-IIn, and they can work in conjunction with CSM interaction. One explanation involves the spin-down of highly magnetized neutron stars, called magnetars, as an additional central-engine energy source to power the light curve (J. P. Ostriker & J. E. Gunn 1971; D. Kasen & L. Bildsten 2010; S. E. Woosley 2010). Another potential central-engine-powered mechanism is the accretion of fallback material onto a black hole (J. Dexter & D. Kasen 2013; T. J. Moriya et al. 2018). A third mechanism involves extremely massive progenitors ($M \sim$ 140–260 $M_\odot$) undergoing thermonuclear explosions triggered by electron–positron pair production, known as pair-instability supernovae (or PISNe; Z. Barkat et al. 1967; S. E. Woosley et al. 2002; A. Heger et al. 2003; S. Schulze et al. 2024).

Unraveling the mysteries surrounding SLSNe-IIn requires detailed comparisons between theoretical models and observations. To that end, comprehensive case studies of individual SLSNe-IIn are still essential. In this paper, we present a large photometric and spectroscopic dataset for SN 2021aaev, followed by a detailed analysis. SN 2021aaev is a SLSN-IIn with peak optical luminosity <-21 mag. We observed

[20] Some interpret SN 2006gy as a Type Ia SN interacting with the circumstellar medium (Ia-CSM); see A. Jerkstrand et al. (2020).

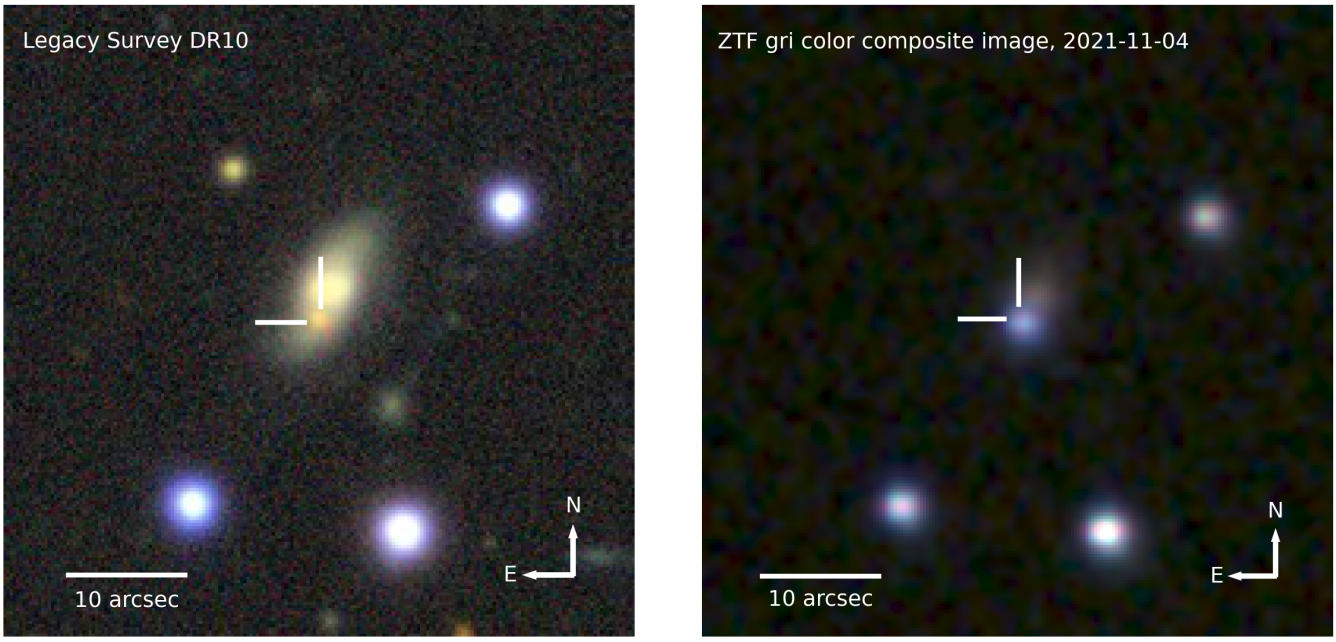

Figure 1. Image of the field of SN 2021aaev. Left: Legacy Survey DR10 *grz* color-composite image of the field of SN 2021aaev before explosion. The location of the SN coincides with a red substructure in the southern part of the host galaxy. We discuss the nature of this red region in Section 6. Right: ZTF *gri* color-composite image of the field of the SN near peak luminosity. The SN has a blue color near peak.

blended, highly ionized flash features during the rise of its light curve and Lorentzian-winged hydrogen Balmer lines throughout all phases. We invoke models with massive and extensive CSM to explain the observed light-curve and spectral features. After the work by T. Kangas et al. (2026) on the SLSN-II flasher with broad Balmer emission SN 2023gpw, SN 2021aaev is the first SLSN-IIn to exhibit flash-ionization features, providing a unique opportunity to explore the diversity within the SLSNe-IIn class.

This paper is organized as follows. In Section 2, we present the photometric and spectroscopic data of SN 2021aaev. In Section 3, we analyze the multiband light curves and compare them both with a SLSN-II sample and with other well-studied luminous H-rich SNe. In Section 4, we investigate the spectral features, focusing on the Lorentzian-winged narrow H lines and the flash features. In Section 5, we model the light curve with common SLSN models. In Section 6, we analyze the host environment using the host spectral energy distribution (SED) and absorption lines. In Section 7, we discuss the CSM properties likely responsible for the superluminous nature of SN 2021aaev, and consider SN 2021aaev's possible relation to other transient types. Finally, Section 8 summarizes the key findings of the paper.

2. Observations

2.1. Discovery

The discovery of SN 2021aaev was first reported on the Transient Name Server (TNS) from the ZTF survey as ZTF21aceqrju (A. Munoz-Arancibia et al. 2021) on 2021 October 10, with R.A. and decl. (J2000.0) $01^{h}23^{m}07\overset{s}{.}825$, $-03°11'13\overset{''}{.}14$. Subsequent analysis of the forced photometry showed that the first detection actually came from the Asteroid Terrestrial-impact Last Alert System (ATLAS; J. L. Tonry et al. 2018) on MJD 59486.43. The potential host galaxy was identified as WISEA J012307.75-031111.3, with a redshift of $z = 0.1557$. This redshift value is derived from the SN narrow emission features and agrees with the redshift derived from host absorption lines (see Section 6.2). On 2021 October 16, SN 2021aaev was classified as a Type II SN (R. Carini et al. 2021) by the Advanced extended Public ESO Spectroscopic Survey of Transient Objects (ePESSTO+; S. J. Smartt et al. 2015) and met the −20 mag threshold for a SLSN-II, with its peak absolute magnitude exceeding −20 mag in the optical bands (see Section 3.1). Since we also observe persistent narrow H lines in the spectra (see Section 4), it is spectroscopically a SLSN-IIn.

Figure 1 shows an image of the field before and after the explosion of SN 2021aaev. Interestingly, the SN location coincides with a red substructure (referred to as the clump hereafter) in the south part of the spiral host. We registered the SN location on its host astrometrically by performing ZTF forced photometry and preexplosion Pan-STARRS *i*-band cutouts of the same field, and identified 12 common reference stars (circled in red in Figure 2). Using IRAF's `imexamine`, we measured the centroids of these stars, derived a transformation between the ZTF and Pan-STARRS images with `geomap`, and applied this transformation to the ZTF SN pixel using `geoxytran`. The SN location in ZTF forced photometry is then projected onto the Pan-STARRS preexplosion image. The uncertainty radius was estimated by adding in quadrature the transformation error (0.64 pixel in *x* and 0.40 pixel in *y*) and the 1σ spread of the ZTF alert positions ($0\overset{''}{.}15$), giving a total uncertainty of about 1.1 Pan-STARRS pixel, or $0\overset{''}{.}28$. As shown in Figure 2, the SN position falls directly on the clump, within the uncertainties. The implications of this peculiar host environment are discussed in Section 6.2.

2.2. Photometry

2.2.1. Optical Photometry from Ground-based Facilities

We obtained multiband optical photometric observations of SN 2021aaev from a variety of ground-based facilities,

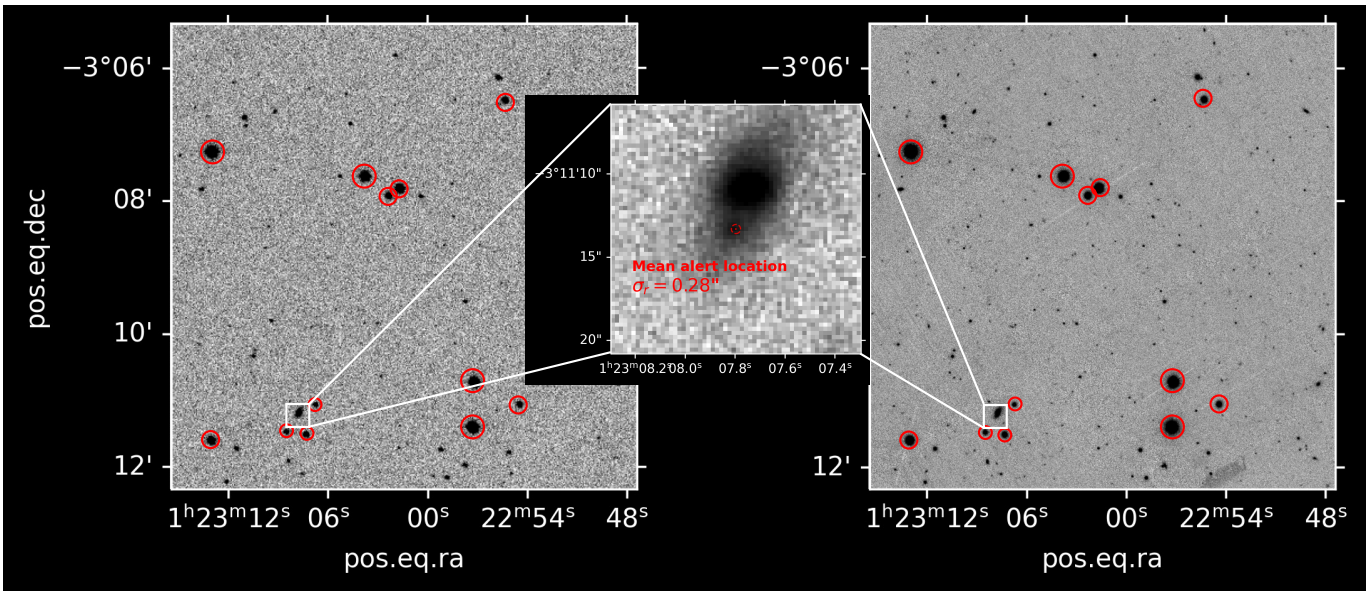

Figure 2. Left: ZTF *i*-band forced photometry cutout of the field around the SN. Circled are 12 common reference stars that also appear in the Pan-STARRS image (see the right) of the same field, which we used for the astrometric registration. Middle: zoomed-in view of the white boxed regions. The SN position in the ZTF image is registered on the Pan-STARRS image, marked by a red dot with the corresponding 1σ uncertainty radius. Right: archival Pan-STARRS *i*-band cutout of the same field.

including ZTF, ATLAS (J. L. Tonry et al. 2018; K. W. Smith et al. 2020), the Spectral Energy Distribution Machine (SEDM; N. Blagorodnova et al. 2018) on the Palomar 60 inch telescope, the Katzman Automatic Imaging Telescope (KAIT) at Lick Observatory (W. D. Li 2000), and the Liverpool Telescope (LT) with the IO:O instrument (I. A. Steele et al. 2004). Observations were taken in the *gri* bands (ZTF, SEDM, LT), *ri* bands (KAIT), and the *c* and *o* bands (ATLAS). The full photometric dataset spans from 2021 September 29 to 2022 November 22, or from −28 to +326 rest-frame days relative to the ATLAS *o*-band peak MJD 59518 (used hereafter; see Section 3.1), and is listed in Table 3. The Milky Way (MW) extinction-corrected photometry (see Section 2.2.3) is shown in Figure 3.

We retrieved the ZTF photometry from the ZTF forced-photometry service (F. J. Masci et al. 2023). For each filter, we performed quality checks, computed the weighted averages of the fluxes on a nightly cadence, and converted fluxes to detection or nondetection limits in the AB magnitude system, as described in F. J. Masci et al. (2023).

The remaining photometry was reduced in a similar fashion. The ATLAS photometry was retrieved from the ATLAS forced-photometry service (L. Shingles et al. 2021) and reduced following the pipeline described in K. W. Smith et al. (2020), which employs point-spread function (PSF)-fitting photometry. Photometry from SEDM and KAIT was processed using the FPipe pipeline (C. Fremling et al. 2016), while the LT photometry was reduced using the IO:O pipeline.[21]

2.2.2. Photometry from Swift/UVOT

We obtained ultraviolet/optical photometry with the 30 cm space-based Ultraviolet/Optical Telescope (UVOT, P. W. A. Roming et al. 2005) on board the Neil Gehrels Swift Observatory (N. Gehrels et al. 2004) in the UVW2, UVM2, UVM1, *U*, *B*, and *V* bands, presented in Figure 3. In 2024 June, we obtained deep images in all filters to remove host contamination from the transient photometry. We coadded all sky exposures for a given epoch to boost the signal-to-noise ratio (S/N) using `uvotimsum` in HEAsoft version 6.32.2.[22] Afterwards, we measured the brightness of the SN with the Swift tool `uvotsource`. The source aperture had a radius of 5″, while the background region had a significantly larger radius. To remove its contribution from the earlier epochs, we arithmetically subtracted the host flux from the early measurements when the SN was bright. The Swift photometry is listed in Table 3.

2.2.3. Absolute Magnitudes

The absolute magnitude M without correcting for host extinction in each filter is given by $M = m - \mu - A_{\mathrm{MW},\lambda} - K_{\mathrm{corr}}$, where m is the apparent magnitude, μ is the distance modulus, $A_{\mathrm{MW},\lambda}$ is the MW extinction at wavelength λ, and K_{corr} is the cosmological K-correction (see, e.g., J. B. Oke & A. Sandage 1968; D. W. Hogg et al. 2002). We computed the distance modulus to be $\mu = 39.426$ mag, using $z = 0.1557$ (see Section 6.2) and assuming a standard flat-ΛCDM cosmology with parameters, given by Planck Collaboration et al. (2020), of $H_0 = 67.66\,\mathrm{km\,s^{-1}\,Mpc^{-1}}$ and $\Omega_{M,0} = 0.31$. We took $E(B-V)_{\mathrm{MW}} = 0.033$ mag,[23] and used the extinction package and `fitzpatrick99` (E. L. Fitzpatrick 1999) extinction law with $R_V = 3.1$ to calculate $A_{\mathrm{MW},\lambda}$ for each filter. The K-correction corrects for differences between the photometric bandpasses in the rest frame and observer frame (D. W. Hogg et al. 2002). Using the available X-Shooter spectrum (see Figure 4), we checked the color term of the K-correction for the UVOT *U* and ZTF *gi* filters, finding corrections of 0.019,

[21] https://telescope.livjm.ac.uk/TelInst/Pipelines/

[22] https://heasarc.gsfc.nasa.gov/docs/software/heasoft

[23] The MW extinction was calculated with the NASA/IPAC Extragalactic Database's (NED) extinction calculator, which uses the E. F. Schlafly & D. P. Finkbeiner (2011) recalibration of the D. J. Schlegel et al. (1998) infrared-based dust map.

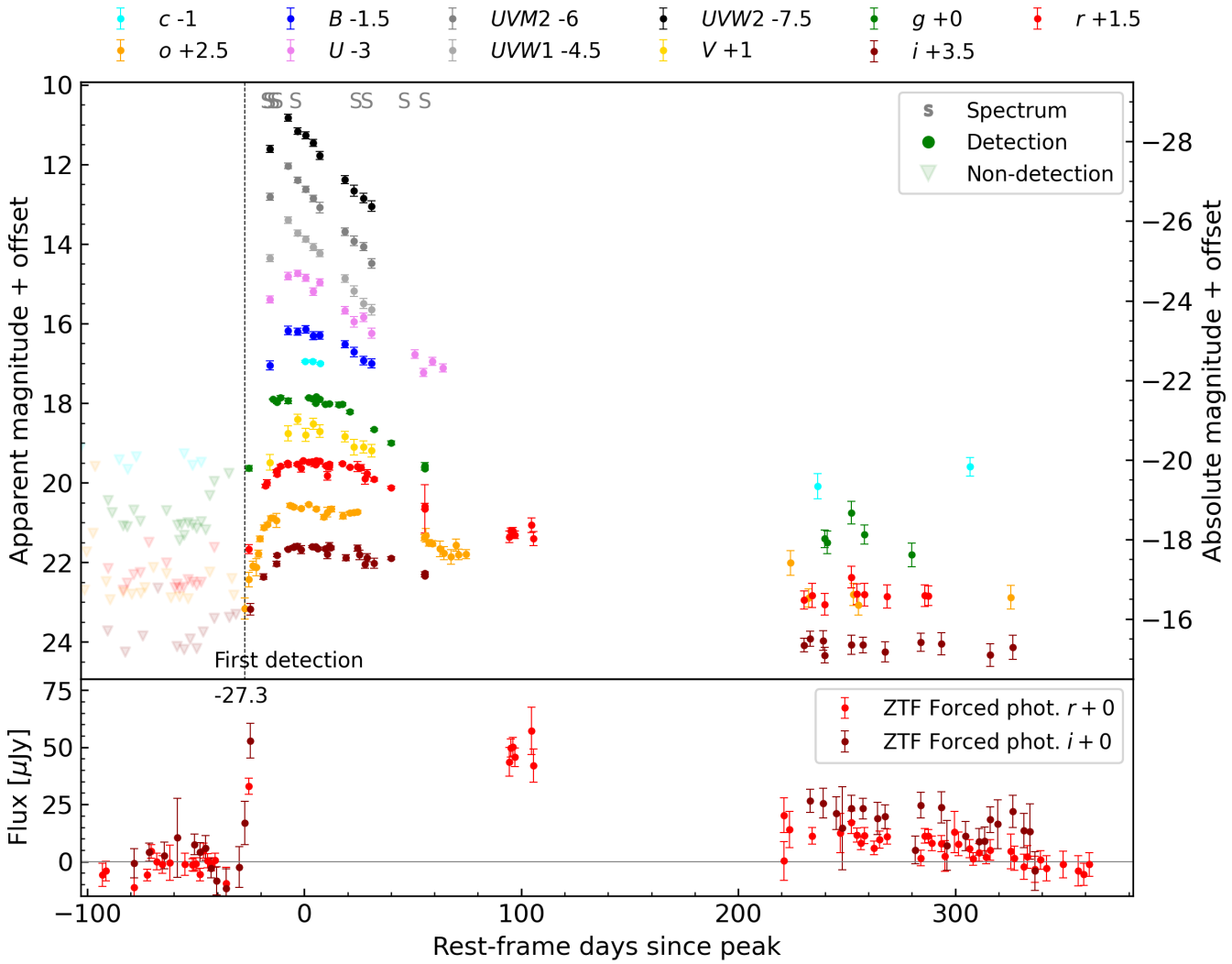

Figure 3. Ultraviolet and optical photometry of SN 2021aaev. The magnitudes are provided in rest-frame days from peak and are corrected for MW extinction. We use a vertical dashed line to mark the first detection. We mark the epochs of spectral observations with "S" symbols at the top of the figure. The bottom panel shows part of the baseline-corrected ZTF *ri* forced photometry. After +250 days, the ZTF *r*- and *i*-band fluxes remained detectable, before dropping to zero near +400 days.

0.024 and 0.022 mag, respectively. These differences are small and the values are negligible compared with the cosmological term of the *K*-correction. Hence, we adopted the cosmological term $-2.5\log(1+z)$ as an approximation for the full *K*-correction, as in Z. H. Chen et al. (2023a) and P. J. Pessi et al. (2025b).

2.3. Spectroscopy

We obtained a total of 13 spectra between 2021 October 10 and 2022 January 3, corresponding to rest-frame days −17.3 to +55.5 relative to the ATLAS *o*-band peak. All spectra were absolutely flux-calibrated using ZTF *gri* photometry in the following way. First, we scaled each spectrum according to the average ratio between each spectrum's synthetic *gri* photometry and the observed ZTF *gri* photometry at the same epoch. Then, a single scale factor was applied to each spectrum accordingly. The epochs of spectroscopic observations are labeled in Figure 3, and the complete spectral sequence is presented in Figure 4. Information about their phases, exposure times, instruments, grisms used, and wavelength ranges can be found in Table 4, and previously unpublished spectra will also be uploaded to the Weizmann Interactive Supernova Data Repository (WISeREP; O. Yaron & A. Gal-Yam 2012).

The first spectrum, obtained during the rise of the SN, was taken with the SPRAT spectrograph (A. S. Piascik et al. 2014) on the 2 m LT. We reduced and flux-calibrated this spectrum using a custom Python pipeline, utilizing the packages Matplotlib (J. D. Hunter 2007), NumPy (S. van der Walt et al. 2011), SciPy (P. Virtanen et al. 2020), and Astropy (Astropy Collaboration et al. 2013). We also used the L.A. Cosmic algorithm (P. G. van Dokkum 2001) to mask cosmic rays. For flux calibration, we used the standard star Hiltner 102 (R. P. S. Stone 1977), which was observed on the same night. Air-mass differences between science and standard star observations were then corrected for using Table 1 from La Palma Technical Note No. 31.[24] Four additional low-resolution spectra were obtained with SEDM (Y. L. Kim et al. 2022), and automatically reduced by pysedm (M. Rigault et al. 2019). However, as these data have very low resolution and do

[24] https://www.ing.iac.es/Astronomy/observing/manuals/ps/tech_notes/tn031.pdf

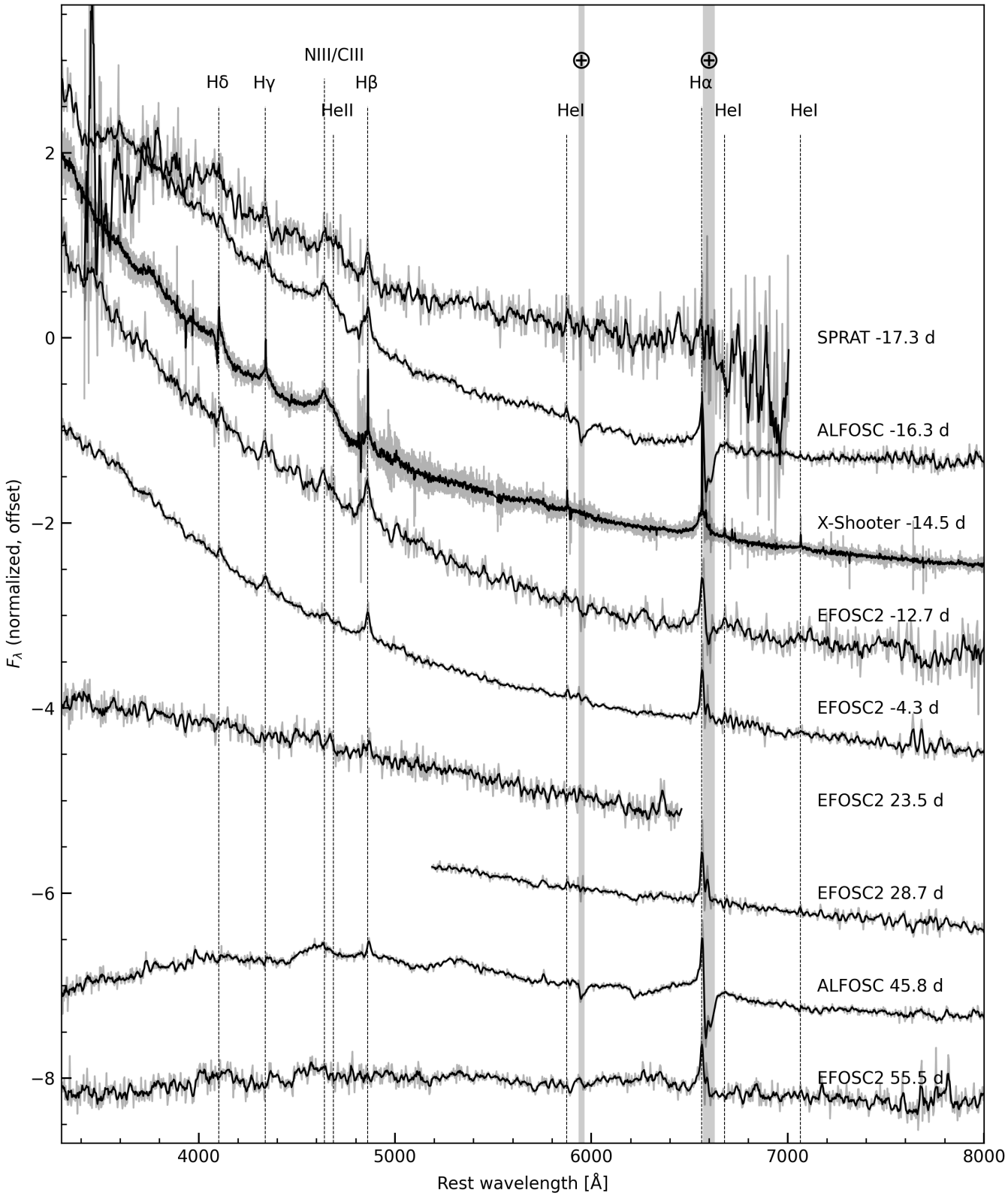

Figure 4. Spectral sequence of SN 2021aaev from −17.3 to +55.5 rest-frame days relative to its ATLAS *o*-band peak. We use vertical lines to identify key features. An offset in flux was applied for illustration purposes. The spectra shown in black are smoothed using a Savitzky–Golay filter, and the original data are presented in lighter colors.

not add significant information on the spectroscopic evolution, they are not included in the analysis presented here but will be uploaded to WISeREP.

Two spectra were obtained with ALFOSC on the 2.56 m Nordic Optical Telescope (NOT). One was taken during the rise using grism 4 and a 1"-wide slit, while the other was taken

postpeak with grism 4 and a 1.″3-wide slit, depending on the observing conditions. Reduction was performed using the PYNOT pipeline in a standard fashion.[25]

We obtained five spectra with the ESO Faint Object Spectrograph and Camera 2 (EFOSC2) on the New Technology Telescope (NTT) at La Silla Observatory as part of the ePESSTO+ program (S. J. Smartt et al. 2015; T.-W. Chen 2019). Observations were made with a 1.″0-wide slit and grisms 11, 13, and 16, and the data were reduced using the PESSTO pipeline.[26] We attempted to correct for telluric absorption with the pipeline, but with varying degrees of success. Consequently, the line profiles on the red side of Hα (gray shaded region) are uncertain. We also stitched spectra from the same day taken with different grisms by averaging overlapping regions.

A higher-resolution X-Shooter spectrum was obtained with ESO's 8.2 m Very Large Telescope (VLT; J. Vernet et al. 2011) at Paranal Observatory. Observations were performed in nodding mode with 1.″0-, 0.″9-, and 0.″9-wide slits for the UV, visible (VIS), and near-infrared (NIR) arms, respectively. The data were reduced following J. Selsing et al. (2019). In brief, we first removed cosmic rays with the tool ASTROSCRAPPY,[27] which is based on the L.A.Cosmic algorithm by P. G. van Dokkum (2001). Afterwards, the data were processed with the X-Shooter pipeline v3.3.6 and the ESO workflow engine ESOREFLEX (P. Goldoni et al. 2006; A. Modigliani et al. 2010). The UVB and VIS-arm data were reduced in stare mode to boost the S/N. The individual rectified, wavelength- and flux-calibrated two-dimensional spectra files were coadded using tools developed by J. Selsing.[28] The NIR data were reduced in nodding mode to ensure a good sky-line subtraction. In the third step, we extracted the one-dimensional spectrum of each arm in a statistically optimal way using the tools developed by J. Selsing. During this step, we also correct for the strongest telluric absorption features of the coadded VIS-arm spectrum with the software package MOLECFIT version 3.3.6 (W. Kausch et al. 2015; A. Smette et al. 2015). Finally, the wavelength calibration of all spectra was corrected for barycentric motion. The spectra of the individual arms were stitched by averaging the overlap regions. We present only the 3500–8000 Å optical spectrum in this paper, as it contains all the information relevant to our analysis. The full X-Shooter spectrum will be made available on WISeREP.

3. Photometric Analysis

3.1. Rest-frame Multiband Light Curves

To characterize the different phases of SN 2021aaev, we converted the time axis to the object's rest frame. The rest-frame time is defined as the interval elapsed since the peak of the ATLAS *o*-band light curve of SN 2021aaev (see Figure 5). The ATLAS *o* band was chosen because it provides the densest coverage during the rise and peak of the light curve.

A smooth curve is required to estimate the peak time of the light curve, which is achieved by interpolating the data. A popular method to perform data interpolation is Gaussian process (GP) regression, a Bayesian approach that models priors as probability distributions over functions. For a comprehensive guide, see C. E. Rasmussen & C. K. I. Williams (2005). We ran a GP regression on each band separately for the multiband dataset.[29] The regression was performed using GEORGE (D. Foreman-Mackey 2015) with a Matérn 5/2 kernel, the result of which shown in Figure 5. To estimate the day of first light, we fit a third-order polynomial to the *o*-band data from the first detection to peak, and solved for its intersection with a baseline from the nondetections (see Figure 6).

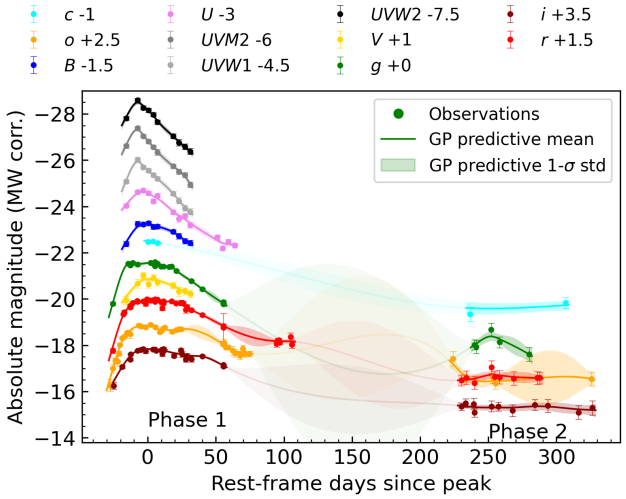

Figure 5. Interpolated multiband light curves of SN 2021aaev using Gaussian process (GP) regression. We interpolated each band separately by a single mean function with a 1σ spread. The predictive variance is large at the solar conjunction phase between phases 1 and 2, so we avoided using interpolation in this gap.

We can now characterize the multiband light curves of SN 2021aaev. In the rest frame, we estimate the first light to be -28.1 ± 1.0 days before the *o*-band peak. In the ATLAS *o* band, the light curve shows an $1/e$ rise time of 25 ± 1 days, with the peak occurring on MJD 59518 ± 1 at an absolute magnitude -21.35 ± 0.03. The peaks in the optical *gri* and *o* bands are smooth. Following this, the *o* band declined on a timescale of 73 ± 1 days to $1/e$ of the maximum flux. Potential bumps are visible in the *o* and *r* bands around days 40–50, but there is no further observational evidence, except for the three epochs of rise in the *o* band following the red cross marked in Figure 6. In the UV, the UVW2 light curve reached its peak at MJD 59509 ± 1, which is 9 days earlier than the optical peak. This peak is much sharper, followed by a faster decline of 21 ± 1 days to $1/e$ of its maximum. No secondary bumps can be identified in the UV bands. A summary of the characterization in the *r*, *o*, and UVM2 bands is presented in Table 1. After solar conjunction, some epochs in the optical were observed with ZTF and ATLAS, labeled as "phase 2" in Figure 5. An apparent bump is seen in the *g* band, possibly due to sparse data and large measurement uncertainties, but no obvious fluctuations or color changes are seen in the *r*-, *o*-, and *i*-band light curves.

[25] https://github.com/jkrogager/PyNOT
[26] https://github.com/svalenti/pessto
[27] https://github.com/astropy/astroscrappy
[28] https://github.com/jselsing/XSGRB_reduction_scripts
[29] Some recent works (e.g., I. Thornton et al. 2023; D. Hiramatsu et al. 2024) have modeled correlations between different bands, performing GP interpolation of all bands in a single run by assigning an effective wavelength to each band. However, little is understood about the color evolution of SLSNe-II, and we do not want to correlate the timescale of the light curve in one band to another. Hence, we did not adapt such a technique.

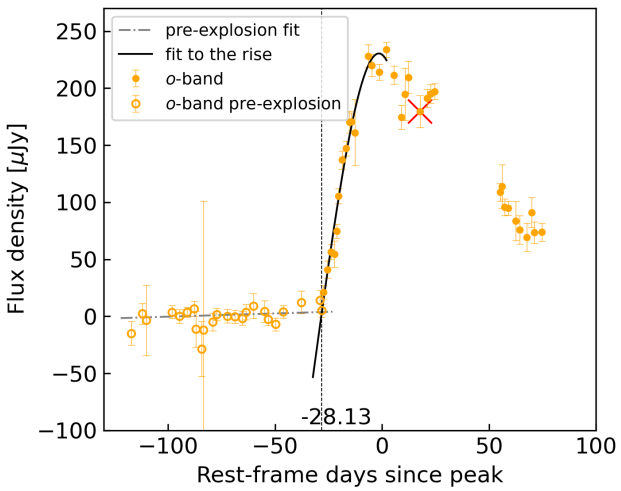

Figure 6. Polynomial fit using the *o*-band photometry to find the day of first light. We fit all detections up to the peak with a third-order polynomial. The preexplosion flux (nondetections in magnitude space) was fit with a straight line. The red cross marks the turning point of a potential bump.

Table 1
Characterization of Key Parameters of the Light Curves for SN 2021aaev in the *r*, *o*, and UVM2 Bands

Parameter	*r*	*o*	UVM2
Peak MJD (day)	59519^{+1}_{-1}	59518^{+1}_{-1}	59509^{+1}_{-1}
Peak mag (mag)	-21.46 ± 0.01	-21.35 ± 0.03	-21.32 ± 0.07
$t_{\mathrm{rise},1/e}$ (day)	22 ± 1	22 ± 1	…
$t_{\mathrm{decline},1/e}$ (day)	54 ± 1	63 ± 1	18 ± 1
$t_{\mathrm{rise},10\%}$ (day)	28 ± 1	27 ± 1	…
$t_{\mathrm{decline},10\%}$ (day)	140 ± 1	126 ± 1	41 ± 1

Note. Other than peak magnitude, all other parameters are estimated in flux space. We conservatively estimate the uncertainty of any time parameters to be ±1 day because the interpolation was performed on every integer MJD. The $t_{\mathrm{rise/decline},1/e}$ or $t_{\mathrm{rise/decline},10\%}$ is defined as the time from/to $1/e$ or 10% of the maximum flux to/from the maximum flux on the rise/decline. We were unable to compute the rise timescale for the UVM2 band because only one point was observed before the peak.

3.2. Light-curve Comparison

We compare the *r*-band light curve of SN 2021aaev with the largest SLSN-II light-curve sample to date in P. J. Pessi et al. (2025b),[30] and show this comparison in Figure 7. SN 2021aaev's *r*-band light curve is distinguished by its higher absolute magnitude but shows unexceptional temporal behavior. We also plot kernel density estimates of the *r*-band peak absolute magnitude as well as the $1/e$ rise and decline times in Figure 8. SN 2021aaev appears luminous in comparison to the median, falling outside the 1σ interval for absolute magnitude. In terms of timescales it is unexceptional. Its slightly faster rise and decline rates are close to the 1σ range of the sample.

We also compare the *r*-band light curve of SN 2021aaev with the r/R-band light curves of other well-studied H-rich, luminous, CSM-interacting SNe, plotted for SN 2006gy, SN 2010jl, and SN 2017hcc in Figure 9. The *r*-band peak of SN 2021aaev is brighter than for SN 2017hcc and perhaps SN 2010jl, but fainter than for SN 2006gy. In terms of timescales, SN 2021aaev has a shorter rise time compared with SN 2017hcc and SN 2006gy (both about 50–60 days). For the decline timescale, SN 2021aaev shows a similar postmaximum decline to SN 2017hcc and SN 2006gy, but all decline faster than SN 2010jl. This is consistent with the results from the comparison with the ZTF SLSN-II sample. All four objects are long-lasting, with SN 2021aaev and SN 2017hcc remaining at −18 mag even 300 days after peak, and SN 2010jl remaining at −18 mag 250 days after discovery. For the three well-studied SNe, massive and/or extensive CSM was invoked to explain the photometry; we expect a similar powering mechanism and CSM properties for SN 2021aaev. CSM-powering models are explored in Section 5.

[30] A slightly different set of cosmological parameters was used in P. J. Pessi et al. (2025b), but this has no significant impact on the inferred light-curve parameters.

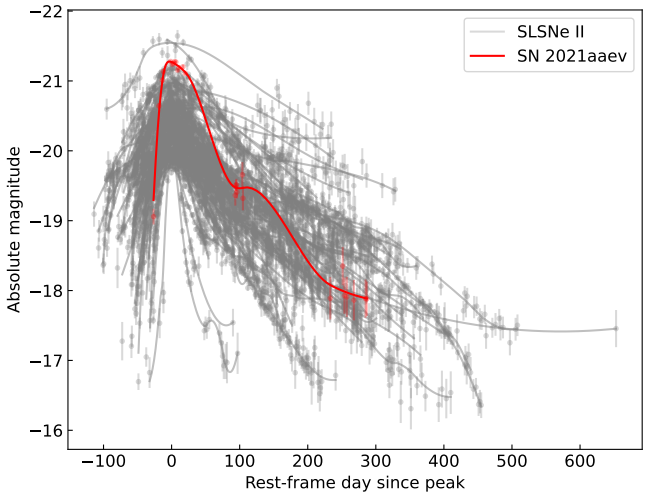

Figure 7. Comparison between the ZTF *r*-band light curve of SN 2021aaev with the rest of the ZTF sample in P. J. Pessi et al. (2025b). All interpolations are done using automated LOESS regression (ALR; Ó. Rodríguez et al. 2019).

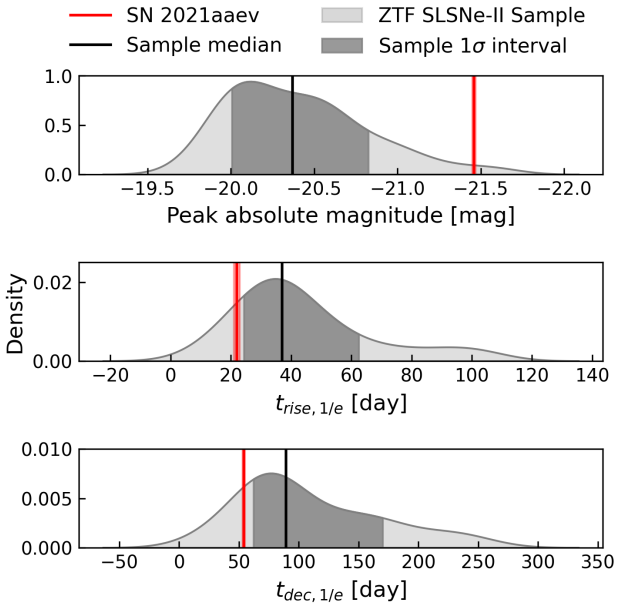

Figure 8. Kernel density estimate of the *r*-band parameters of the ZTF sample in P. J. Pessi et al. (2025b), with the black vertical line indicating the sample mean and SN 2021aaev marked by the red vertical line.

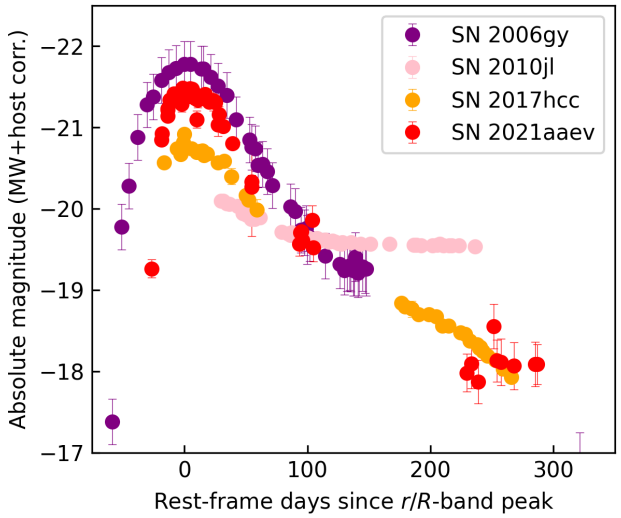

Figure 9. Comparison of the *r*-band light curve of SN 2021aaev with those of SN 2017hcc (S. Moran et al. 2023), SN 2010jl (e.g., C. Fransson et al. 2014), and SN 2006gy (*R* band; see N. Smith et al. 2007). The photometry for SN 2010jl and 2006gy is corrected for host extinction, while SN 2017hcc and 2021aaev has negligible or undetermined host extinction.

3.3. Pseudo-bolometric Light Curve, Temperature, and Radius

We constructed a pseudo-bolometric light curve for SN 2021aaev from its UV and optical light curves in the following way. We selected epochs with observations in at least two bands, resulting in a total of 34 such epochs. For these 34 epochs, we used the observed bands and GP values for unobserved bands to fit blackbody curves and determine the blackbody temperature. These bands covered about $\lambda =$ 2000–8000 Å. For extrapolations, a blackbody tail was attached to the NIR up to $\lambda = 24000$ Å, and a blackbody curve to the far-UV (FUV) end down to $\lambda = 1000$ Å using the aforementioned temperature. To acquire luminosity values, we connected points with straight lines between $\lambda = 2000$–8000 Å, and also integrated the area under the extrapolated blackbody curves. The total luminosity of that epoch is then the sum of these areas (see Figure 10). The UV-optical blackbody-corrected pseudo-bolometric light curve from this construction is shown at the top of Figure 11.

The pseudo-bolometric light curve of SN 2021aaev peaks at 2.62×10^{44} erg s^{-1}, 9 days before the ATLAS *o* band, and the total energy released as radiation is estimated to be 1.4×10^{51} erg. This level of radiative output is in principle attainable via standard core-collapse explosion mechanisms alone, such as a delayed neutrino-driven explosion (H.-T. Janka 2012). However, achieving such a high radiative efficiency would require a substantial fraction of the ejecta's kinetic energy to be converted into radiation. In the presence of a dense CSM, this conversion can occur efficiently through shock interaction, which serves as a mechanism to tap into the kinetic energy reservoir of the ejecta. From a simple kinetic perspective, efficient energy conversion requires a strong deceleration of the ejecta, which favors a "heavy" CSM scenario where the mass of the CSM is comparable or even exceeds that of the SN ejecta (see, e.g., E. O. Ofek et al. 2014; D. K. Khatami & D. N. Kasen 2024). This is discussed in Section 5.

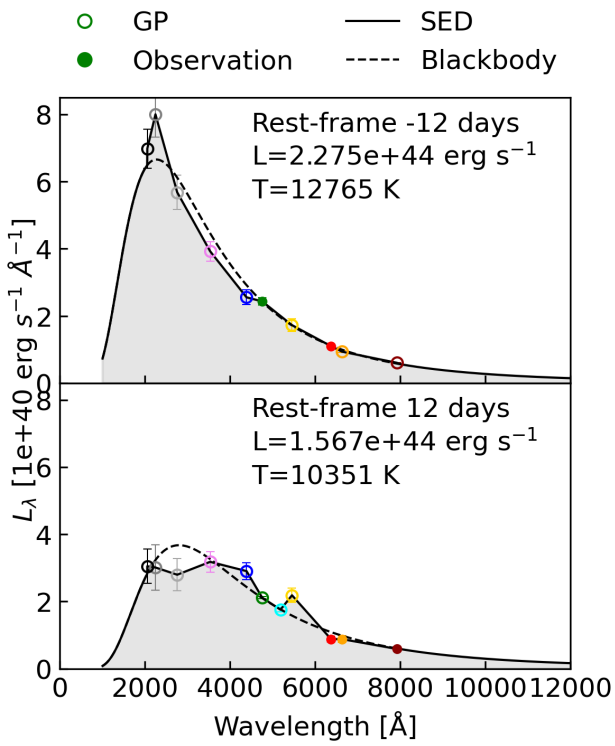

Figure 10. The SED of SN 2021aaev, using one epoch before peak (−12 days) and one epoch after peak (+12 days) as examples. The total luminosities are corrected with a FUV (from 1000 Å) and a NIR (to 24000 Å) blackbody. The colors for the filters are the same as those in Figure 5.

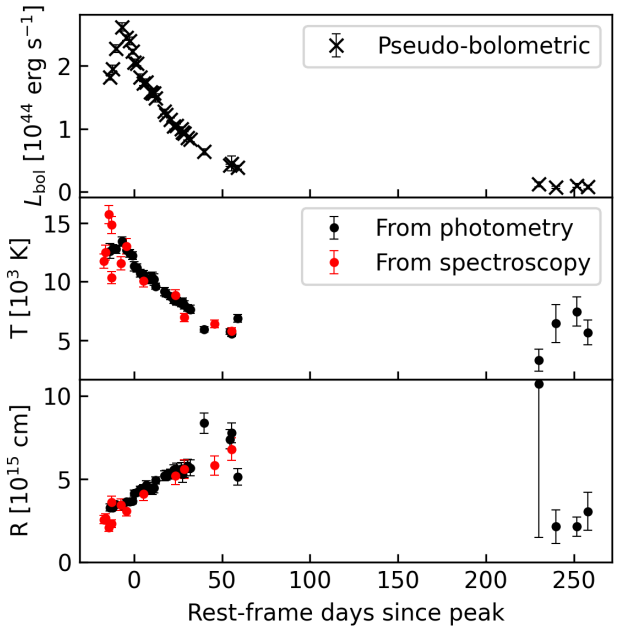

Figure 11. Top: UV-optical (2000–8000 Å) pseudo-bolometric light curve of SN 2021aaev, corrected using a blackbody fit to the FUV (from 1000 Å) and the NIR (to 24000 Å). Middle and bottom: photospheric blackbody temperature and radius evolution of SN 2021aaev from its multiband photometry and absolute-calibrated spectra (see Section 4).

When fitting the blackbody, we also obtained the evolution of the estimated photospheric blackbody temperature and radius, as shown in Figure 11. These estimates help trace the

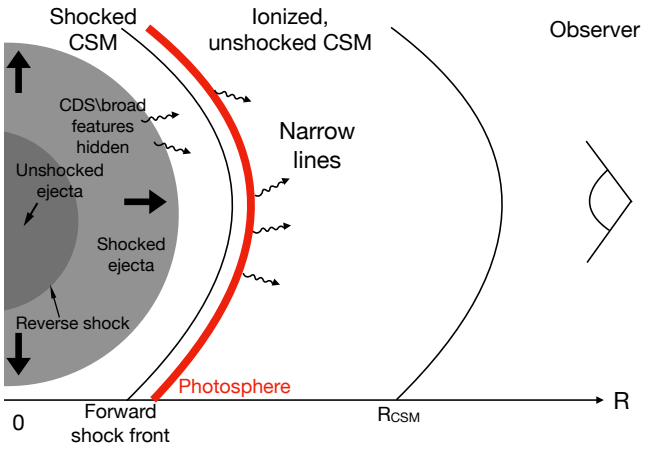

Figure 12. An illustration of the SN line-emitting regions and photosphere evolution. After the onset of the CSM interaction, the photosphere is located in the unshocked CSM and expands as the shock wave travels outwards. The narrow lines are flash and Balmer lines in the first ∼20 days, and Balmer lines only in the later photospheric phase. A forward–reverse shock structure with a cold dense shell (CDS) in between is expected to form, but it remains unseen because the photosphere lies beyond it during these epochs.

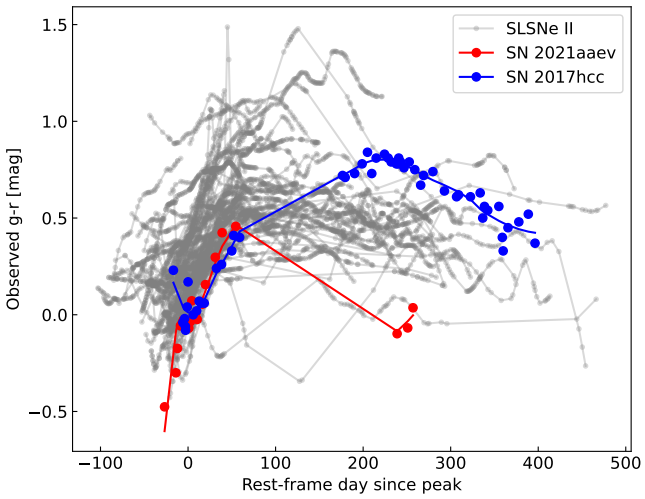

Figure 13. The ZTF $g - r$ color evolution of SN 2021aaev, SN 2017hcc (S. Moran et al. 2023), and the SLSN-II sample in P. J. Pessi et al. (2025b). All interpolations are done using ALR (Ó. Rodríguez et al. 2019).

thermal and geometric evolution of the emitting region over time. The temperature and radius derived from spectroscopy (presented in Figure 4) are also included in the plot, and are generally consistent with those derived from photometry. The blackbody temperature follows a similar evolutionary trend as the pseudo-bolometric light curve, peaking near the UV maximum (rest frame −8 days) at approximately 15,000 K and declining to around 5000 K by +50 days. The high temperature during the early phase suggests a substantial UV contribution, which is characteristic of SLSNe. This is consistent with the flash-ionization features observed (see Section 4.2) and is a sign of intense interaction with CSM. Meanwhile, the blackbody photospheric radius expands until approximately rest frame +50 days. During this phase, the photosphere is located in the unshocked CSM, and continues to expand as more of the CSM becomes ionized and optically thick due to the ongoing shock interaction (e.g., R. A. Chevalier & C. Fransson 1994), reflecting the expansion of the ionized region. In the standard ejecta–CSM interaction framework, the shock structure consists of a forward shock propagating into the CSM and a reverse shock propagating back into the ejecta. If the shocks are radiative, efficient cooling leads to the formation of a cold dense shell (CDS; e.g., N. N. Chugai et al. 2004) between the two shocks. Given the strong signs of interaction in SN 2021aaev, such a CDS is likely present. However, during the epochs probed the photosphere is located in the unshocked CSM, so any CDS would remain hidden observationally. For an illustration of this structure, see Figure 12.

3.4. Color Evolution

We calculated the $g - r$ color of SN 2021aaev and plot its evolution in Figure 13. For comparison, we include SN 2017hcc and SLSNe-II from the ZTF sample in P. J. Pessi et al. (2025b). The data adopted the $-2.5\log(1+z)$ cosmological K-correction term. However, the data at late phases are generally poorly sampled and carry large uncertainties; thus, the plot should be considered only as an indication of the general trend in the color evolution. SN 2021aaev evolves from a relatively blue $g - r$ color of approximately −0.5 mag at ∼−30 days to a redder color of 0.5 mag by ∼70 days. At very late times (>250 days), the color declines again, falling to around −0.1 mag.

Compared to other SLSNe-II in the ZTF sample, SN 2021aaev exhibits a relatively blue early photospheric phase, suggesting a higher blackbody temperature (15,000 K). Despite this, its early-time color evolution is broadly consistent with the rest of the ZTF sample. Notably, at late times (≳200 days), SN 2021aaev becomes significantly bluer while most SLSNe-II, such as SN 2017hcc, maintain a redder plateau. There are several possible explanations for this. First, such a trend is seen in some SNe II (see, e.g., Y.-P. Yang et al. 2024) during the radioactive ^{56}Ni-powered tail. However, if this reversion to blue is because of radioactive decay, it would require an implausibly large ^{56}Ni mass ($\gtrsim 7\,M_\odot$; M. Nicholl 2021) to sustain SLSN-like luminosities of $L \sim 10^{44}$ erg s^{-1}, well above typical core-collapse yields. Second, a similar blueward shift was observed in SN 2017hcc at a later phase (+230–460 days), attributed to the emergence of a forest of Fe II lines that affect broadband photometry (by contributing to the bluer filters; S. Moran et al. 2023); we also tentatively identify a blend of Fe II lines in SN 2021aaev in the +84.9 days spectra (see Figure 14). Third, this reversion to bluer colors may reflect renewed heating of the photosphere, driven by ongoing or renewed CSM interaction. Because of the strong spectral evidence for CSM interaction (see Section 4) and the presence of Fe II, the latter two reasons are the more likely explanations for the late-time reversion to blue in SN 2021aaev.

4. Spectroscopic Analysis

4.1. Spectral Evolution

The full spectral sequence of SN 2021aaev is presented in Figure 4. A selection of spectra are presented and compared with spectra of well-studied SNe IIn and SLSNe-IIn in Figure 14. In this section, we will use days since first light for easier comparison. A strong telluric line falls onto the red side of the Hα of SN 2021aaev. This affects the reliability of the red side of the Hα profile in most spectra, although successful telluric correction has been applied to the +15.3 days X-Shooter spectrum.

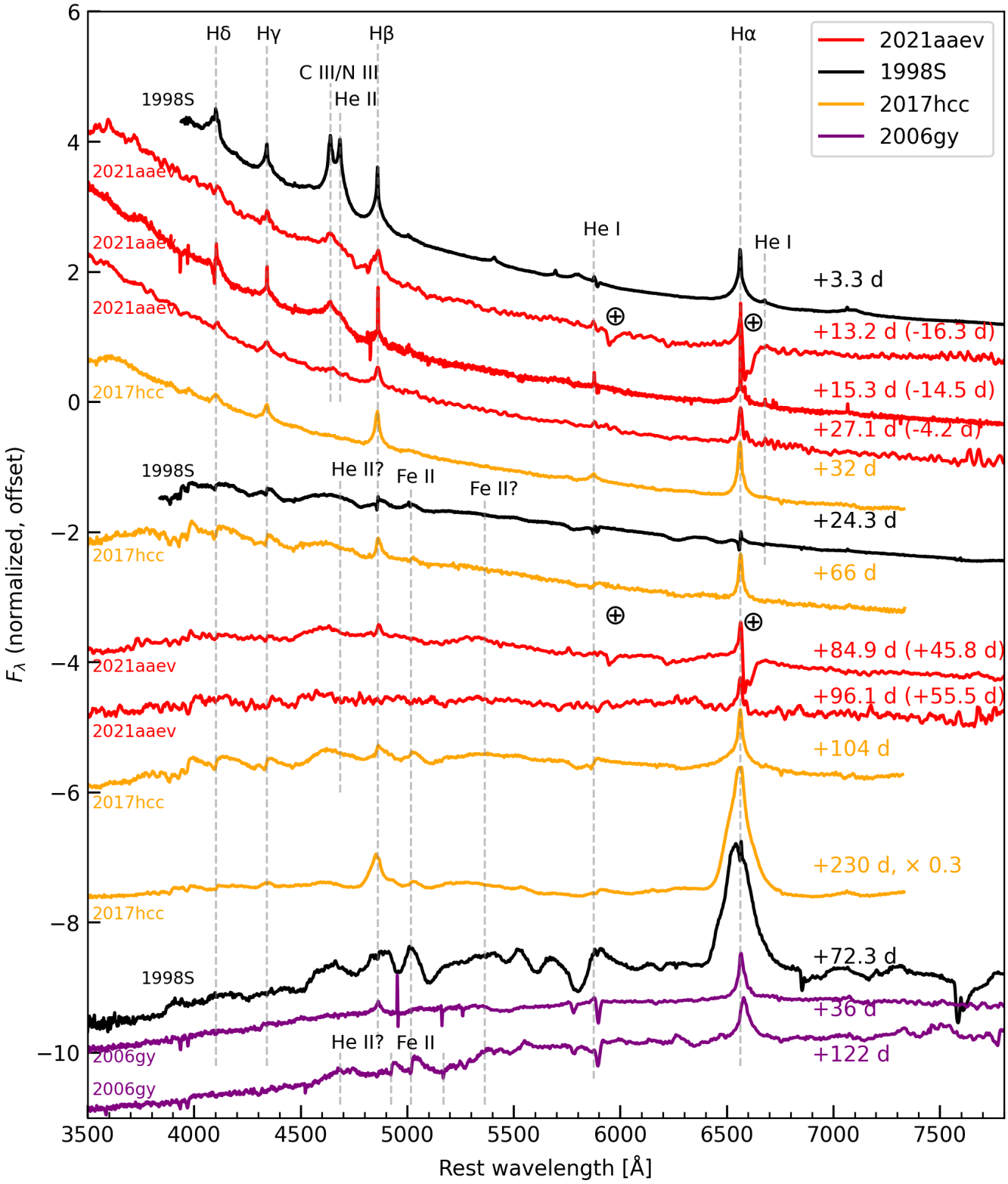

Figure 14. Spectral evolution of SN 2021aaev compared with the H-rich, superluminous SN 2006gy and SN 2017hcc, and a SN-IIn flasher SN 1998S. All fluxes are normalized with respect to the continuum near Hα. The phases without brackets represent days since first light of each SN, while the phases with brackets indicate rest-frame days relative to the maximum light for SN 2021aaev.

In the early photospheric phases (up to +27.1 days), the spectra are characterized by a blue continuum and Lorentzian-winged narrow Balmer lines. The blue continuum comes from the hot, optically thick, expanding photosphere located in the ionized CSM. No ejecta features are observed. This spectral morphology is common among SNe IIn in their early

photospheric phase, where narrow emission lines arise from slow-moving CSM beyond the photosphere and are broadened into Lorentzian wings via electron scattering (see Section 4.3 for details). We illustrate our understanding of the physical structure of the SN at this phase in Figure 12. During this phase, there is also an evolving feature around 4600 Å, which we identify as resulting from flash ionization (possibly a blend of C III λ4649, N III $\lambda\lambda$4634, 4641, and He II λ4686). However, the flash features in SN 2021aaev show no doubly peaked narrow components, in contrast to many other flash spectra, e.g., the +3.3 days spectrum of SN 1998S. This is discussed in Section 4.2.

As the spectra evolve toward maximum light, the flash feature begins to fade and is hardly visible by +27.1 days. At a comparable phase, the first spectrum of SN 2017hcc (+32 days) closely resembles the +27.1 days spectrum of SN 2021aaev, with no identifiable flash features. SN 2006gy, on the other hand, has a much redder early-time spectrum (+36 days) compared with its photometrically similar counterparts. Following this phase, a broad feature, likely photospheric He, appears at about 4500–4600 Å. This broad feature has been observed in the +66 to +104 days spectra of SN 2017hcc, and is also present in some SNe IIn, albeit at a much earlier phase (e.g., +24.3 days in SN 1998S). In the +84.9 days spectra of SN 2021aaev, we tentatively identify a forest of Fe lines blending into a broad feature between 5000 and 5500 Å; Fe II features are also seen in the +66, +104 and +230 days spectra of SN 2017hcc and the +122 days spectrum of SN 2006gy.

The Hα line in the +84.9 and +96.1 days spectra remains narrow and strong, with no evidence of broadening. This behavior contrasts with that of many less luminous SNe IIn in their late photospheric phase, where broad features from the ejecta begin to emerge (e.g., +72.3 days in SN 1998S), though exceptions exist, e.g., SN 1994W (J. Sollerman et al. 1998; N. N. Chugai et al. 2005; L. Dessart et al. 2009) and SN 2009kn (E. Kankare et al. 2012). At the +84.9 days, the spectral evolution of SN 2021aaev closely resembles that of SN 2017hcc. The persistence of narrow Balmer lines in both cases indicates continued CSM interaction at these late phases, and suggests that the ejecta have been strongly or entirely decelerated, implying $M_{\rm CSM} \geqslant M_{\rm ej}$.

4.2. Flash-ionization Features

We observe blended flash-ionization features of He II λ4686 and possibly C III λ4649/N III $\lambda\lambda$4634, 4641 in the early photospheric phase of SN 2021aaev. These highly ionized lines provide strong evidence for the presence of dense and confined CSM (A. Gal-Yam et al. 2014; D. Khazov et al. 2016), and typically last for only a few days during the rise phase (O. Yaron et al. 2017; R. J. Bruch et al. 2023). Flash features are commonly observed in H-rich SNe, with estimates indicating that at least 30% of all H-rich SNe display such signatures when early spectra are available (R. J. Bruch et al. 2023). SN 2021aaev is the first SLSNe-IIn with observed flash spectroscopy. Another SLSN-II (with broad Balmer lines), SN 2023gpw, also exhibits flash features (estimated peak r-band magnitude $= -21.47$ mag; T. Kangas et al. 2026).

While the He II λ4686 flash feature in many other flashers exhibits distinct narrow components, no such components are observed in SN 2021aaev. In addition, the He II λ4686 feature in SN 2021aaev appears consistently weaker than the nearby

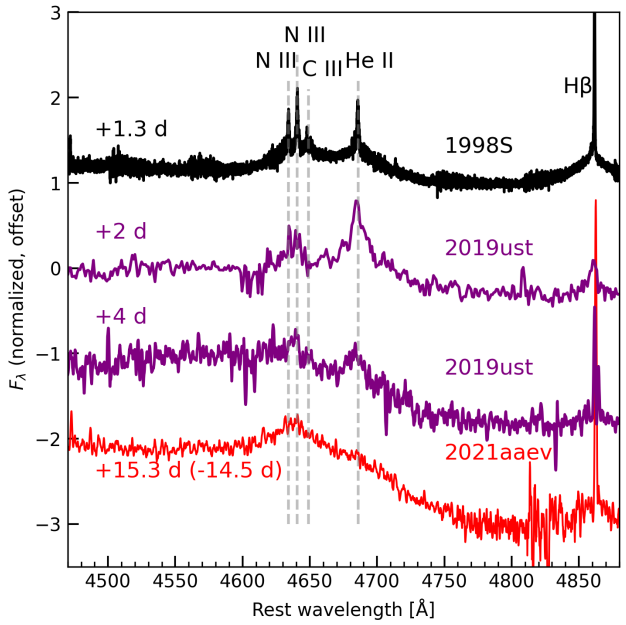

Figure 15. He II λ4686 and C III λ4649/N III $\lambda\lambda$4634, 4641 flash features of SN 2021aaev, as compared with those of SN 1998S and SN 2019ust. The flash features in SN 2019ust evolve and broaden, suggesting that a similar process may have occurred in SN 2021aaev, with the broad flash features seen in the X-Shooter spectrum representing a later stage of such evolution.

feature at ∼4645 Å in all observed flash spectra, whereas in many other flashers (see, e.g., the first spectrum of SN 1998S in Figure 14), the He II line is comparably strong, if not stronger. This may indicate that the flash features caught in SN 2021aaev were at a later phase (∼15 days since first light) in comparison to most other flashers. For instance, the evolution of SN 2019ust (R. J. Bruch et al. 2023) in Figure 15 shows that this flash feature is fast evolving, and broadens and weakens as time progresses. Broad flash features are sometimes referred to as "ledge" features (see, e.g., M. T. Soumagnac et al. 2020; J. Pearson et al. 2023) and are explained as either blueshifted He II λ4686 (A. Gal-Yam et al. 2011) or a blend of other highly ionized C, N, and O lines (L. Dessart et al. 2017). We favor the second explanation for SN 2021aaev, as no additional high-velocity features are present in the spectra at a similar phase.

The long flash timescale observed in SN 2021aaev is also noteworthy. R. J. Bruch et al. (2023) compiled a "golden flasher" sample of H-rich SNe, in which they defined the flash timescale as the duration from first light to the midpoint between the last flash spectrum and the first nonflash spectrum. However, this definition may not be appropriate for the superluminous SN 2021aaev and SN 2023gpw, both of which lack early spectral coverage. In the case of SN 2021aaev, there is a 10 days gap between first light and the earliest flash spectrum obtained with SPRAT, and a similar situation applies to SN 2023gpw (T. Kangas et al. 2026). To improve this estimate, we redefine the start of the flash timescale for the two SLSNe-II as the midpoint between first light and the first flash spectrum, rather than using first light directly. This revised estimate still places SN 2021aaev and SN 2023gpw among the longest flashers (both about 24 days), as shown in Figure 16.

R. J. Bruch et al. (2023) found correlations between the flash timescale, peak luminosity, and rise time. We added

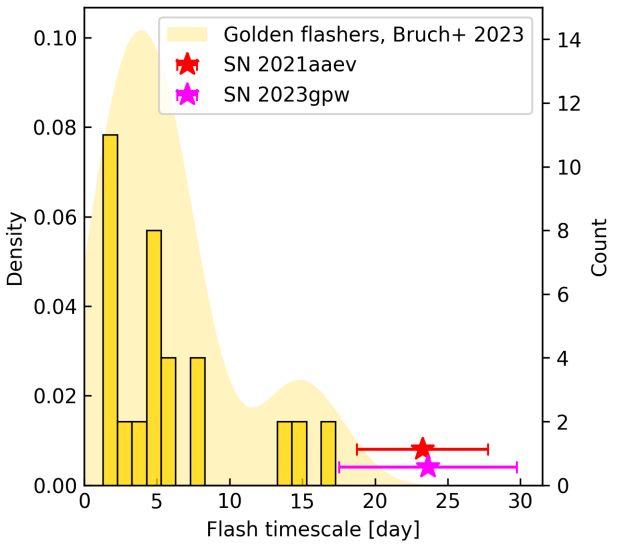

Figure 16. Kernel density estimate and histogram of the flash timescale of the golden flasher sample (R. J. Bruch et al. 2023) and SN 2021aaev and SN 2023gpw.

SN 2021aaev and SN 2023gpw to their correlation plots (see Figure 17) and recalculated the relationships. The two SLSN-II flashers have much longer rise times and brighter peaks than most objects in the golden flasher sample, but they still follow the trend. For peak magnitude versus flash timescale, we obtained a Pearson correlation coefficient of -0.827 ($p = 0.000004$). For rise time versus flash timescale, we obtained a Pearson correlation coefficient of 0.748 ($p = 0.0001$). Both indicate strong correlations that may reflect underlying dependencies on the mass and radial extent of the CSM. However, the sample remains too small to draw definitive conclusions, in particular for the SLSN-II class.

4.3. Electron Scattering

Quantitative information on the optical depth of flash features in CSM can be extracted by modeling their Lorentzian wing broadening as a result of electron scattering. Photons emitted from the forward-shock front scatter off free electrons in the CSM, leading to broadened line profiles. A Monte Carlo code, ESCATTER,[31] has been developed to model Hα line profiles under the assumption that the CSM follows a single power-law density profile, $\rho = \rho_0 r^{-s}$. It has been applied to SLSNe-II such as SN 2021adxl (S. J. Brennan et al. 2024).

We assume that for SN 2021aaev the broadening seen in the flash features and Hα (with a velocity dispersion of $1399 \pm 38\,\mathrm{km\,s^{-1}}$) in the -14.5 days X-Shooter spectrum arise from the same electron-scattering process. For Hα, we neglect the narrow component and compare the Lorentzian wings with a grid of ESCATTER models with Thomson optical depths ranging from 1 to 20 (left of Figure 18). Models with lower optical depths ($\tau = 1, 2$) agreed best with the observed Hα profile. For the blended flash feature, we assume that the broadening has a contribution from the He II λ4686 line as well as a second contribution from an unidentified line (possibly C IIIλ4649 or N III λ4634, averaged to 4641). We compare the observed profile with an ESCATTER model with $\tau = 3$ (right panel of Figure 18), arbitrarily scaling the two model lines' amplitudes while keeping their separation fixed. Although a blue deficit exists in the model, it otherwise agrees well with the observations.

From the above analysis, we conclude that the two Lorentzian-winged features seen in the X-Shooter spectrum of SN 2021aaev originate from regions with slightly different radial optical depths. The blended flash features likely arise from a somewhat deeper layer, in the ionized, unshocked CSM just outside the forward shock, where the UV flash from shock breakout ionizes the material and electron scattering shapes the line profiles. The CSM must be dense enough to produce scattering wings, but not so dense as to obscure the flash completely, consistent with a moderately optically thick, extended CSM environment.

5. Light-curve Modeling

Building on the photometric and spectroscopic analyses presented above, we now attempt to construct a self-consistent picture of SN 2021aaev. We explore possible light-curve models that can explain the powering of SN 2021aaev and are consistent with the conclusions from the spectral analysis.

5.1. Analytical CSM-interaction Models

We searched for generic analytical models that are applicable to an extensive CSM-interaction-powered SLSNe. D. K. Khatami & D. N. Kasen (2024) introduced an analytical framework to fit light curves of CSM-interaction-powered SNe, under the assumptions that the inner CSM edge is much smaller than the outer edge and the ejecta reach homologous expansion before colliding with the CSM. In this framework, the "shock breakout" is defined as the moment when the forward-shock front reaches a low enough optical depth for photons to escape, while the moment that the shock exits the CSM entirely is referred to as "shock emergence." Two key parameters are introduced: a mass ratio $\eta = M_{\rm CSM}/M_{\rm ej}$ and a "breakout" parameter ξ, which depends on η as well as the outer radius of the CSM $R_{\rm CSM}$ and the initial ejecta velocity $v_{\rm ej}$. These define four light-curve regimes: heavy ($\eta > 1$) or light ($\eta < 1$) CSM, and breakout at the edge ($\xi > 1$) or interior ($\xi < 1$).

To interpret the long timescale and sustained luminosity of SN 2021aaev, we adopt the interior shock-breakout regime (schematic diagram shown in Figure 19), which is consistent with the spectroscopic evidence for prolonged CSM interaction. We fit the interior breakout analytical scaling relations presented in D. K. Khatami & D. N. Kasen (2024, Section 3) to the bolometric light curve, adopting $\kappa_e = 0.34\,\mathrm{cm^2\,g^{-1}}$, and apply the correction factors from D. K. Khatami & D. N. Kasen (2024, Figure 17) derived from numerical simulations. Since we did not observe a shock emergence phase for SN 2021aaev, corresponding to $t_{\rm SE}$ in Figure 19, we set the estimated shock emergence earlier limit to the last observed photometry epoch and assign a large uncertainty of 200 days. The model involves seven free parameters: $M_{\rm CSM}$, $M_{\rm ej}$, $R_{\rm CSM}$, $v_{\rm ej}$, the CSM density exponent s, the outer ejecta density exponent n, and a breakout exponent k_0, where $k_0 = 0$ refers to edge breakout and $k_0 = 1$ to immediate breakout once the interaction begins. However, degeneracies exist between the parameters, especially between $M_{\rm ej}$ and $v_{\rm ej}$. Due to the absence of broad ejecta features, such as P-Cygni profiles or

[31] https://github.com/eScatter/e-scatter

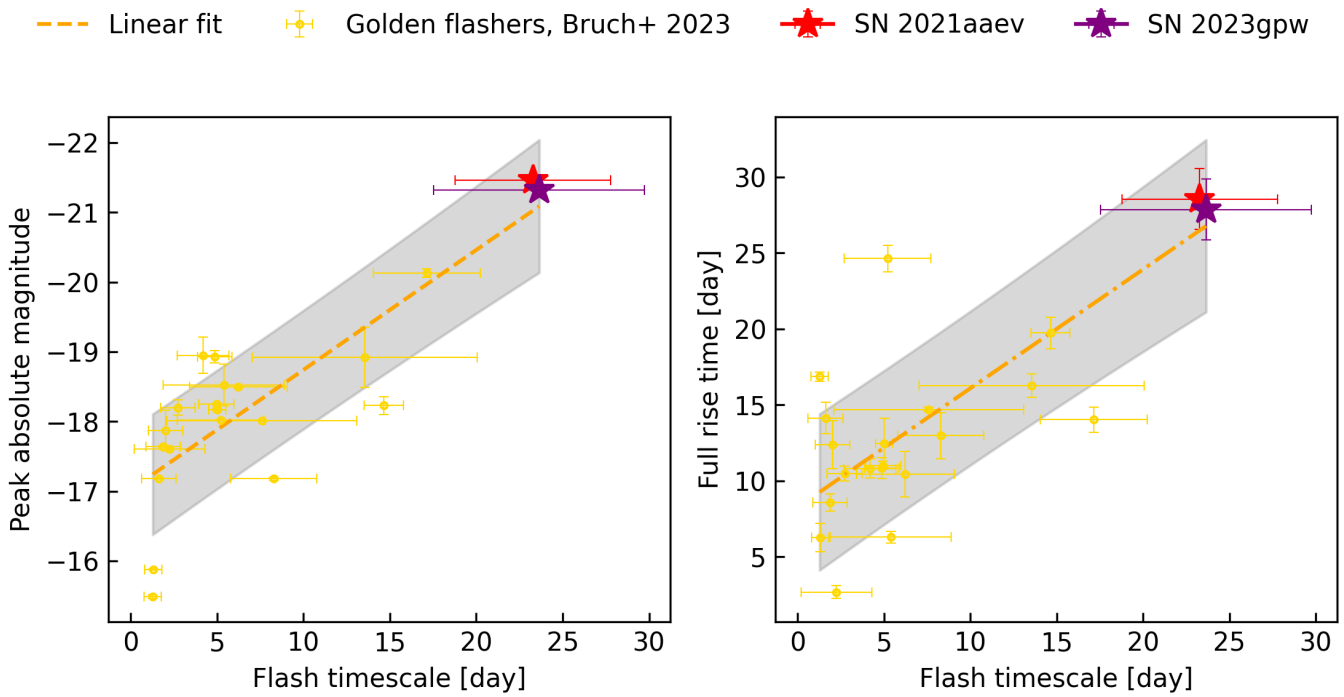

Figure 17. Left: flash timescale vs. peak absolute magnitude in the r band. Right: flash timescale vs. rise time in the r band. The plots build on Figure 16 in R. J. Bruch et al. (2023), with the extra additions of SN 2021aaev and SN 2023gpw (T. Kangas et al. 2026). The gray zones denote 1σ intervals.

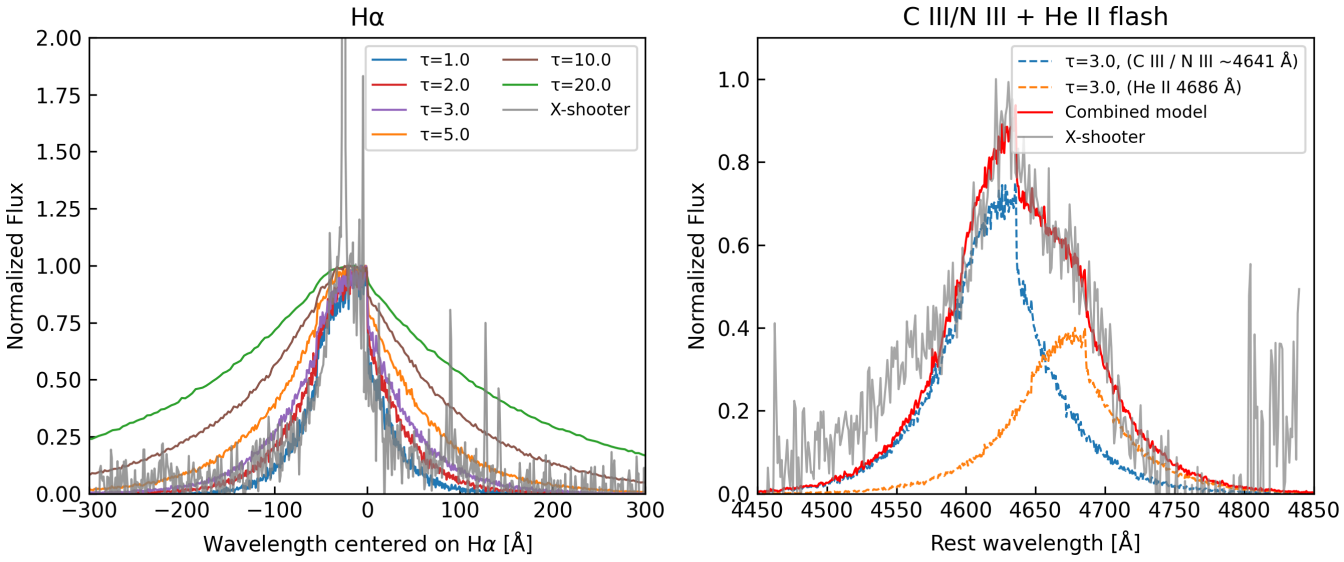

Figure 18. Comparison between observed Lorentzian-winged features in the X-Shooter spectrum of SN 2021aaev and models generated by ESCATTER. The code allows one to change the wind velocity v_w, shock velocity v_s, and CSM density exponent s, but these parameters do not impact the line profile. We fixed them as $v_w = 100\,\mathrm{km\,s^{-1}}$, $v_s = 2500\,\mathrm{km\,s^{-1}}$, and $s = 2$. Left: observed Hα and a grid of line profile models with different Thomson optical depths τ. Right: observed blended flash features at 4600–4700 Å and two arbitrarily scaled line profile (with fixed separation) models with $\tau = 3$.

nebular-phase emission lines, we cannot directly infer the ejecta velocity from observations. Therefore, to improve the inference, we fixed $n = 10$ and $v_{ej} = 11{,}000\,\mathrm{km\,s^{-1}}$, which is typical for CCSNe. We further applied uniform priors of $M_{CSM} \in [0, 25]\,M_\odot$, $M_{ej} \in [0, 25]\,M_\odot$, $R_{CSM} \in [1 \times 10^{14}, 5 \times 10^{16}]$ cm, $k_0 \in [0.59, 1]$, and $s \in [0, 3]$.

We find that the best-fit (median) scenario is for an ejecta of $M_{ej} = 1.34^{+0.06}_{-0.06}\,M_\odot$ colliding with a CSM of $M_{CSM} = 12.9^{+3.8}_{-3.9}\,M_\odot$ and $R_{CSM} = 1.57^{+0.35}_{-0.29} \times 10^{16}$ cm, shown in the left panel of Figure 20 (corner plot shown in Figure 25). This result is also summarized in the first row of Table 2. The fitted bolometric light curve matches the breakout peak and captures the overall trend of decline well (with a slight overshoot). This clearly supports the heavy-interior regime, where the SN ejecta collides with a more massive CSM, continuously interacting with the CSM and depositing most of the kinetic energy into radiation (with an

Table 2
Best-fit Parameters of Various Models for SN 2021aaev

Model	ϵ	$M_{\rm ej}$ ($M_\odot$)	$v_{\rm ej}$ (10^3 km s^{-1})	$M_{\rm CSM}$ ($M_\odot$)	$R_{\rm CSM}$ (10^{16} cm)	k_0	s	B_p (10^{14} G)	P_0 (ms)
CSM*	0.87	$1.34^{+0.06}_{-0.06}$	11	$12.9^{+3.8}_{-3.9}$	$1.57^{+0.35}_{-0.29}$	$0.85^{+0.10}_{-0.11}$	$1.55^{+0.98}_{-1.02}$	...	...
CSM**	0.60	$1.96^{+0.09}_{-0.08}$	11	$14.4^{+4.4}_{-4.1}$	$1.78^{+0.36}_{-0.31}$	$0.85^{+0.10}_{-0.10}$	$1.51^{+1.03}_{-1.04}$	...	...
Magnetar	...	$1.17^{+0.05}_{-0.05}$	$9.85^{+0.13}_{-0.14}$	...	...	...	...	$1.53^{+0.96}_{-0.45}$	$3.95^{+0.56}_{-0.56}$

Note. CSM*: the "heavy-interior" analytical CSM-interaction model in D. K. Khatami & D. N. Kasen (2024). CSM**: the same CSM-interaction model with an additional constraint that the energy conversion efficiency $\epsilon = 0.60$. Magnetar: the magnetar-powering model in M. Nicholl et al. (2017), implemented using REDBACK (N. Sarin et al. 2024).

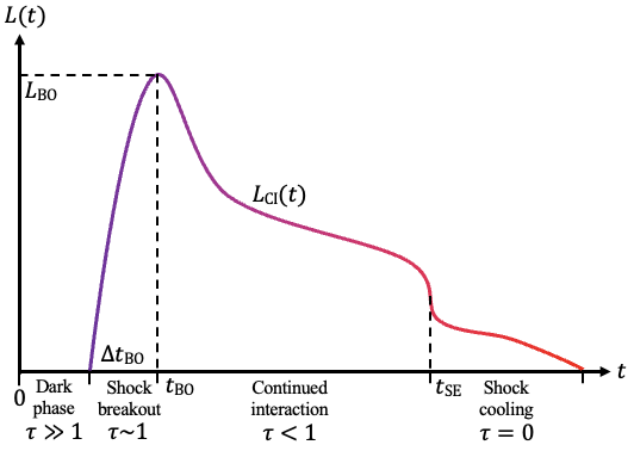

Figure 19. Schematic diagram illustrating the different phases of a CSM-interaction-powered SN light curve, adapted from D. K. Khatami & D. N. Kasen (2024) for the interior breakout scenario. Initially the shock front is in an optically thick dark phase. As the shock propagates radially outward it transitions into an optically thin region, and shock breakout is witnessed inside the CSM with sharply rising luminosity. Then, the continued CSM–ejecta interaction powers the light curve. At $t_{\rm SE}$, we would see the light curve plummet as the shock emerges from the CSM edge.

efficiency calculated as $\epsilon = 0.87$). Spectral evidence supports the existence of a continued interaction phase up to +96.6 days since first light, with narrow Hα and Hβ lines persisting but decreasing in strength during the decline of the light curve. This physical picture is also consistent with the electron-scattering analysis in Section 4.3. The shock-breakout phase corresponds to epochs in which flash features are present and the optical depth transitions from $\tau \gg 1$ to $\tau \sim 1$. Beyond this phase, $\tau < 1$, and the extensive windlike CSM density may no longer be sufficient to support an observable flash, such that no flash features are expected thereafter.

Nevertheless, the simple analytical model presented above has many limitations. First, the derived kinetic energy of $E_{\rm KE} = 1.62 \times 10^{51}$ erg would require an exceptionally high energy conversion efficiency of 0.87. If we impose the additional constraint that the conversion efficiency $\epsilon = 0.6$ (close to that of SN 2006gy inferred in D. K. Khatami & D. N. Kasen 2024) by scaling the numerical factors simultaneously in the analytical model, then the median model corresponds to an ejecta of $M_{\rm ej} = 1.96^{+0.09}_{-0.08}\,M_\odot$ colliding with a CSM of $M_{\rm CSM} = 14.4^{+4.4}_{-4.1}\,M_\odot$ and $R_{\rm CSM} = 1.78^{+0.36}_{-0.31} \times 10^{16}$ cm; see the right panel of Figure 20 (corner plot shown in Figure 26). This does not change the "heavy-interior" conclusion, but the fit is in general poorer. Second, the constraint on s is weak, meaning that we cannot use this model to accurately estimate the density profile of the CSM. Another limitation is that it does not provide any quantitative prediction on the rising part of the light curve. A more detailed modeling of the rising light curve and CSM density profile, e.g., similar to the approach presented in S. P. Cosentino et al. (2025) for a low-mass CSM, could be pursued in future work to improve our understanding of the shock–CSM interaction in SN 2021aaev.

As a comparison we also fit the multiband light curve with the commonly used semi-analytical CSM-interaction model of E. Chatzopoulos et al. (2013), implemented as the `csm` model in REDBACK (N. Sarin et al. 2024). Using broad priors of $M_{\rm CSM} \in [0, 100]\,M_\odot$, $M_{\rm ej} \in [0, 200]\,M_\odot$, and $v_{\rm ej} \in [10^3, 10^5]$ km s^{-1}, the best-fitting solution yields extremely large masses of $M_{\rm ej} = 141.8^{+4.2}_{-4.3}\,M_\odot$ and $M_{\rm CSM} = 10.3^{+0.3}_{-0.5}\,M_\odot$, with an ejecta velocity of $v_{\rm ej} = 5384^{+84}_{-62}$ km s^{-1}.[32] Such an enormous ejecta mass is incompatible with realistic core-collapse progenitors, and we regard this solution as less physically motivated than the model in D. K. Khatami & D. N. Kasen (2024) discussed above.

5.2. Magnetar Model

The spin-down of a magnetar is another commonly invoked powering mechanism to explain the light curves of SLSNe. We fit the light curve of SN 2021aaev with the magnetar model from M. Nicholl et al. (2017). This model is also available in REDBACK as the `slsn` model, which is a magnetar model that fits multiband light-curve data with the constraints that the magnetar rotational energy is larger than the total output energy and that the nebula phase does not begin for at least 100 days. We performed nested sampling with default priors $M_{\rm ej} \in \log U[0.1, 100]\,M_\odot$, $v_{\rm ej} \in \log U[0.1, 100]\,10^3$ km s^{-1}, $P_0 \in U[1, 10]$ ms, and $B_p \in \log U[0.1, 10]\,10^{14}$ G. The best-fit parameters are listed in Table 2 and a comparison of the observed multiband data is shown in Figure 21.

The best-fit magnetar model reproduces the overall amplitude and trend of the *gri- and o*-band light curves, but fails to capture the postpeak small-scale aperiodic fluctuations. The fit is notably poorer in the bluer bands, particularly at early phases. We infer a spin period P_0 of 3.95 ms and a magnetic field strength of 1.53×10^{14} G, both of which are consistent with the reported values in the literature for SLSNe-I (e.g., ~2.5 ms and $0.2-18 \times 10^{14}$ G; M. Nicholl et al. 2017). The inferred ejecta mass of $1.17\,M_\odot$ is however much lower than the median ejecta mass ($5.03^{+4.01}_{-2.39}$) of magnetar-powered SLSNe in Z. H. Chen et al. (2023b), but still within the plausible range. We conclude that the spin-down of a magnetar remains a viable mechanism for powering the generic

[32] When narrower priors are adopted, the Markov Chain Monte Carlo chains simply run against the prior bounds, indicating that extreme values are intrinsically preferred in this inference case.

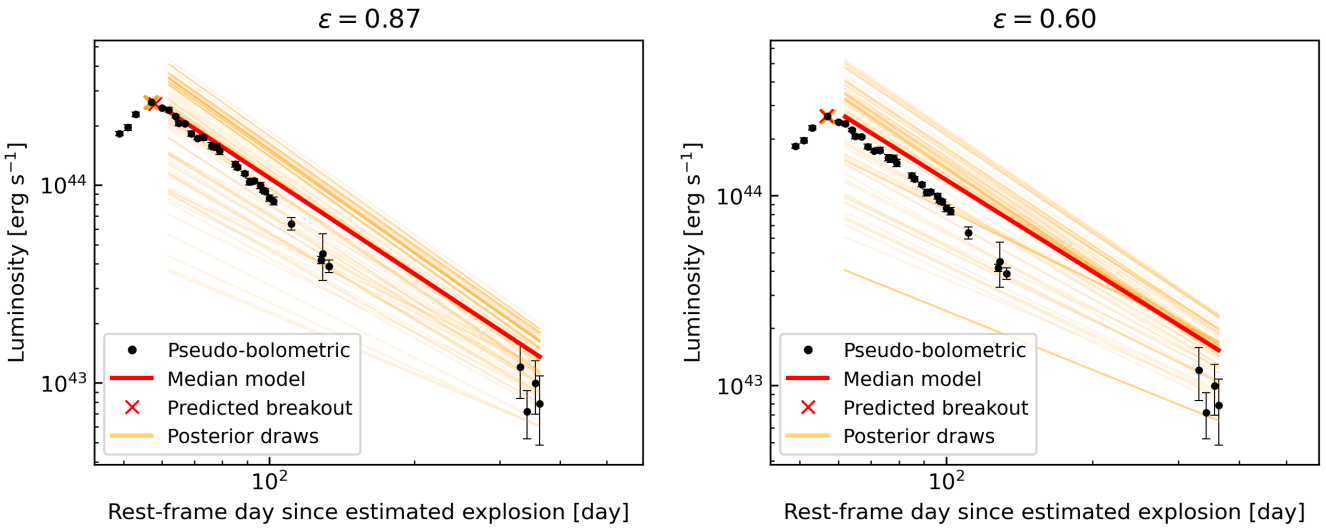

Figure 20. Left: comparison between the bolometric light curve constructed from observed photometry and analytical models in D. K. Khatami & D. N. Kasen (2024), with no constraint on energy conversion efficiency ϵ. The best-fit model gives $\epsilon = 0.87$. Right: the same model with an additional constraint that $\epsilon = 0.60$. We draw the plots in log–log scale for better visualization.

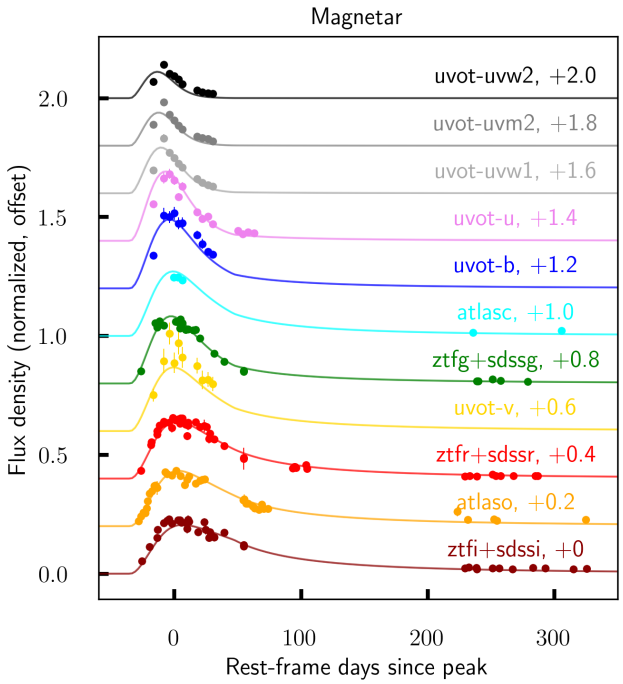

Figure 21. Fitting the multiband photometry of SN 2021aaev with the magnetar model from M. Nicholl et al. (2017). The fitting was implemented using REDBACK (N. Sarin et al. 2024).

light-curve evolution of SN 2021aaev, but fails to capture the color changes during the rise. Moreover, magnetar-powering models alone cannot account for the aperiodic bumpy optical light curves or the persistent narrow emission lines seen in the spectra.

6. Host-galaxy Environment

6.1. Host SED Modeling

The SED and physical properties of the underlying host can provide further constraints on the progenitor and environment

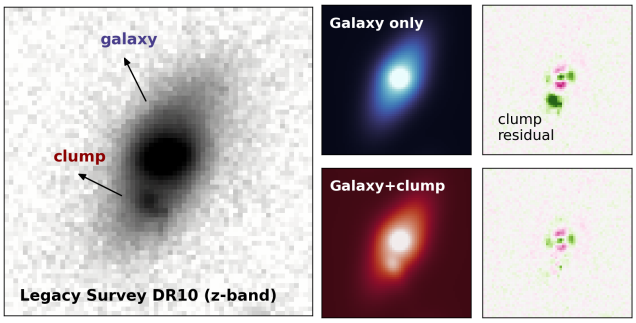

Figure 22. Morphological modeling of the SN 2021aaev host. The left panel shows the Legacy Survey DR10 z-band image of the system (15″ × 15″), highlighting the location of the central spiral galaxy and the accompanying clump, whose position coincides with the SN 2021aaev explosion. The middle panels plot the best-fit PYSERSIC models when only the galaxy (upper) or the galaxy+clump morphologies (lower) are considered. The right panels show the residual of each fit; the presence of the clump is clearly revealed in the upper residual plot.

of SN 2021aaev (e.g., S. Schulze et al. 2021). A red, green, blue (RGB) composite of the host galaxy of SN 2021aaev is shown in Figure 1, which appears to be a spiral galaxy. The SN is coincident with a red substructure in the southeastern part of the galaxy (the aforementioned clump).

We opt to decompose and study the SED of the spiral galaxy and the clump separately. First, we use the Bayesian inference code PYSERSIC (I. Pasha & T. B. Miller 2023) to characterize the morphology of the galaxy+clump system. We model the central galaxy using a double Sérsic profile with coincident centers and position angles but allowing the effective radius, Sérsic index, and ellipticity to vary, in order to better capture the two-dimensional light distribution of the bulge and the spiral arms altogether. The southern clump is modeled simultaneously to the spiral using a point source. This procedure is applied to *griz* images of the system available from the Legacy Survey Data Release 10 (DR10), and PSF models are constructed for each band from stacked images of stars in the field. Altogether, this method allows us to accurately extract the morphology of the galaxy and the clump at the same time (see Figure 22). Even

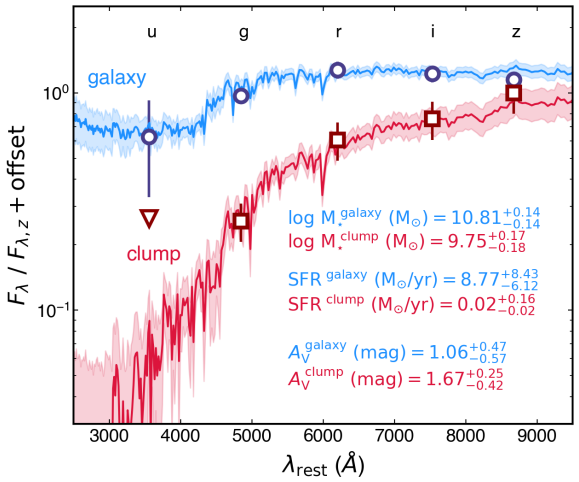

Figure 23. SED decomposition and physical properties of the system hosting SN 2021aaev. The extracted photometry and SED fits for both the spiral galaxy and the underlying clump are shown in blue and red, respectively, with the shaded band encompassing the 16th–84th percentile range for the best-fit SEDs drawn from the BAGPIPES realizations. The mean stellar mass, SFR, and optical extinction are listed in the inset for each component (with uncertainties).

though the apparent color of the clump may be compatible with MW stars in the foreground, the residual images reveal that the clump is resolved in the *iz* photometry, excluding this possibility. In view of these results, we model the morphology of the clump in these two bands (*iz*) using an independent Sérsic profile, and repeat the fitting. This results in an effective (or half-light) radius for the clump of $r_{\rm eff}^{\rm clump} = 3\farcs8 \pm 0\farcs3$ (2.7 ± 0.2 kpc) in the *z* band, around 3 times smaller than the extent of the spiral companion of $r_{\rm eff}^{\rm galaxy} = 12\farcs9 \pm 0\farcs1$ (9.0 ± 0.1 kpc).

Importantly, the morphological decomposition enables us to deblend the flux contributions of the spiral galaxy and the red clump from the total flux of the system (see Figure 22). The observed SED of the spiral galaxy is given by the amplitude (i.e., integrated flux) of the best-fit double Sérsic model, while the photometry of the clump is given by the total flux of the point source in the *gr* bands and by the best-fit single Sérsic model in the *iz* bands. Using weight maps of each image, PYSERSIC returns errors on these morphological parameters, which we adopt as our uncertainties in the flux. In order to better constrain the current star formation rate (SFR) of the system, we also consider the *u*-band exposures from SDSS Data Release 18 using the same methods, although we acknowledge that the clump is not visible in the latter, and accordingly a 5σ limit on the flux is reported for this filter.

We can subsequently derive constraints on the SED properties of the galaxy and the clump (namely stellar masses $M_\star$ and star formation histories, SFHs) by fitting the available ground-based photometry (*ugriz*) with the Bayesian Analysis of Galaxies for Physical Inference and Parameter EStimation code, or BAGPIPES (A. C. Carnall et al. 2018). BAGPIPES uses the updated G. Bruzual & S. Charlot (2003) stellar population synthesis templates with a P. Kroupa (2001) stellar initial mass function. In fitting the data, we adopt an exponentially declining prior for the SFH. We allow for a broad range of stellar masses and *e*-folding times for the burst duration, and an age interval limited to the age of the Universe at the redshift in question. For simplicity, and given the modest number of photometric points, the metallicity is fixed to the solar abundance value. We use a D. Calzetti et al. (2000) dust-attenuation law, with the *V*-band optical depth allowed to vary between $0 \leqslant A_V \leqslant 2$ mag.

The observed photometry, best-fit SEDs, and derived physical properties for the galaxy and clump are presented in Figure 23. With a stellar mass of $\log(M_\star^{\rm clump}/M_\odot) \simeq 9.8$, the clump contributes more than 10% to the total mass of the system, and is significantly redder ($A_V^{\rm clump} \simeq 1.7$ mag), while the galaxy is compatible with lower extinction ($A_V^{\rm galaxy} \simeq 0.9$ mag) and a higher stellar mass of $M_\star^{\rm galaxy} \simeq 10.6\,M_\odot$. Remarkably, the spiral galaxy is still forming stars at an active pace (SFR $\simeq 5.47\,M_\odot\,{\rm yr}^{-1}$), while the clump ceased forming stars long time ago. Given the clump's substantial mass, distinct SED, and size compared with the main galaxy, the clump may represent a dwarf satellite galaxy or a merging companion with an old stellar population.

6.2. Host-galaxy Lines

We observed the Mg II $\lambda\lambda$2797, 2803 doublet (saturated), the Mg I λ2852 line, the Ca II H (λ3968) and K (λ3934) lines, and the Na I D $\lambda\lambda$5890, 5896 doublet in the −14.5 days X-Shooter spectrum, as shown in Figure 24. These lines are commonly associated with absorption in the interstellar medium of the host galaxy, and all are consistent with a redshift of $z = 0.1557 \pm 0.0001$. Interestingly, the Mg II doublet exhibits secondary blueshifted components, corresponding to a velocity offset of 139 ± 21 km s^{-1}. This is consistent with the two-component host environment that we see in Figure 1 and the interpretation that the clump may be a dwarf satellite galaxy or a merging companion.

The equivalent width of the Na I D $\lambda\lambda$5890, 5896 doublet is related to galaxy extinction. Using the empirical relation from D. Poznanski et al. (2012), we derive a MW extinction of $E(B-V)_{\rm MW} = 0.033 \pm 0.012$ mag and a host extinction of $E(B-V)_{\rm host} = 0.086 \pm 0.032$ mag, resulting in a total extinction of $E(B-V) = 0.119 \pm 0.044$ mag. The MW extinction is consistent with the value from NED's extinction calculator, within uncertainties (see Section 2.2.3). While the inferred host reddening is nonnegligible, the relation assumes that the extinction comes from a diffusive interstellar source rather than circumstellar dust. In the case of SN 2021aaev, a SLSN-II with clear signs of CSM interaction, the local environment may also contain dusty CSM, which can contribute to the overall reddening in a way not captured by this relation. Given this ambiguity, we opt not to apply a host-extinction correction for photometric analysis.

The narrow H lines observed in the X-Shooter spectra can resemble those originating from the host-galaxy H II regions. To investigate this, we analyzed the velocity dispersions of the Mg I, Ca II, and Na I lines, finding values around 30 km s^{-1}. The narrow Hα component gives a velocity dispersion of 39 ± 1 km s^{-1}, and the Hβ lines exhibit velocity dispersions of 29 ± 2 km s^{-1}. Given that the resolution of the X-Shooter VIS arm is $R = 8900$ for a 0\farcs9 slit width, these emission features are all resolved and consistent with the typical velocity dispersions observed in extragalactic H II regions (J. R. Roy et al. 1986). However, we did not observe strong [O III] or [O II] lines relative to the H lines. The Balmer decrement in the X-Shooter spectrum gives a value of 1.4, which is inconsistent with that of a typical H II region. Considering these discrepancies with H II region emission, along with other evidence indicating the presence of CSM (see

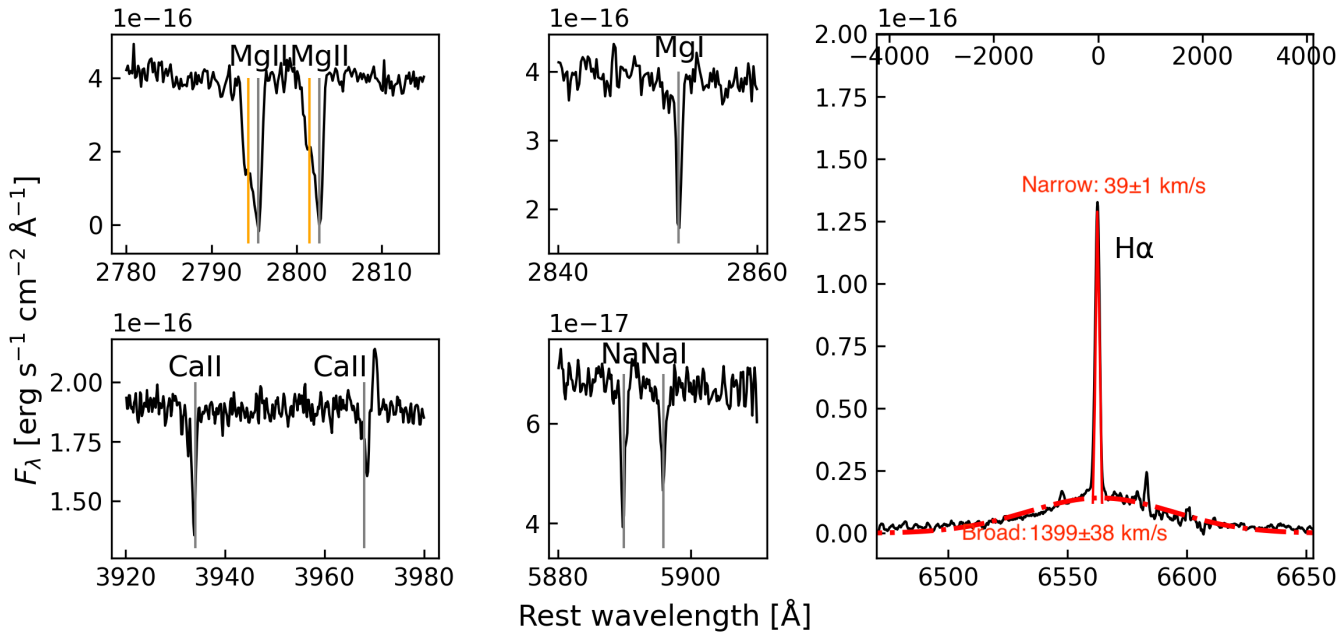

Figure 24. Potential host lines seen in the rest-frame −14.5 days X-Shooter spectrum of SN 2021aaev. We identified host Mg I, Mg II, Ca II, and Na I lines. The gray vertical lines are consistent with a redshift of $z = 0.1557 \pm 0.0001$, and the orange lines have a relative velocity of 139 ± 21 km s^{-1} compared with the gray lines. A narrow Hα component at $z = 0.1557 \pm 0.0001$ is visible, but further analysis points toward interaction with CSM rather than emissions from a host H II region.

Section 4.2), we conclude that the majority of the narrow Balmer-line component in X-Shooter can be attributed to CSM rather than the host.

7. Discussion

7.1. What CSM Properties Make SN 2021aaev Superluminous?

SN 2021aaev stands out as an extremely luminous H-rich interacting SN, with a peak luminosity 3 orders of magnitude brighter than that of some SNe IIn, such as SN 1998S, which is also thought to be primarily powered by interaction with CSM. This raises a key question: What CSM properties enable SN 2021aaev to become superluminous?

The most important physical parameter that characterizes the ejecta–CSM interaction is perhaps the mass ratio between the CSM and ejecta. From SN 2021aaev, we observed light-curve and spectral evidence of long-lived CSM interaction, with no identifiable ejecta features for up to approximately 100 days after first light. This implies that the ejecta were constantly buried within an optically thick CSM and experienced significant deceleration. The degree of deceleration is closely related to the mass ratio between the CSM and ejecta. This parameter also governs the energy conversion efficiency, where a larger $M_{\rm CSM}/M_{\rm ej}$ ratio generally gives a higher efficiency. However, energy conversion efficiency does not necessarily increase monotonically with CSM mass for a given ejecta kinetic energy. As argued by D. K. Khatami & D. N. Kasen (2024), there may exist an optimal mass ratio near unity that maximizes radiative output. Beyond this point, further increases to CSM mass merely decelerate the ejecta. In the case of SN 2021aaev, which has an inferred CSM–ejecta mass ratio of ∼9, the conversion efficiency may already be somewhat suppressed relative to this optimum. Nonetheless, our analytical model in Section 5 demonstrates that a CSM exceeding the ejecta in mass provides a viable explanation for the pseudo-bolometric light curve of SN 2021aaev. This scenario also naturally extends to other luminous, slowly evolving H-rich interacting SNe with comparable peak luminosities and timescales, such as SN 2017hcc, SN 2006gy, and SN 2010jl. In contrast, events such as SN 1998S may involve lower $M_{\rm CSM}/M_{\rm ej}$ ratios, resulting in less efficient energy conversion and faster light-curve evolution. Still, a handful of well-studied cases is insufficient to answer whether SLSNe-IIn are merely the luminous tail of the SN-IIn population. A more systematic, sample-based approach, incorporating both photometry and spectroscopy, is needed to address this question robustly.

Another key parameter is the radial extent of the CSM. In SN 2021aaev, spectroscopic evidence points to a complex, extended, and perhaps stratified CSM configuration. The coexistence of persistent narrow Balmer emission lines and early-time flash-ionization features with broad Lorentzian wings suggests a radially layered CSM. Specifically, the transient flash features around 4650 Å, attributed to He, N, and/or C, imply the presence of a compact, dense inner shell. This is a phase in which the interaction physics may differ from other phases (see, e.g., T. Matsuoka et al. 2025), while the persistent narrow Balmer components originate from more extended, photoionized H-rich material that remains unshocked. This structure likely reflects a history of episodic pre-SN mass-loss events, transitioning from a continuous, wind-driven outflow to more explosive or eruptive ejections closer to core collapse.

Given this inferred massive, extensive CSM, what can we say about the preexplosion activities and the progenitor of SN 2021aaev? The inferred CSM mass is comparable to that of SN 2006gy, which required a ∼10–20 $M_\odot$ CSM to explain its luminosity and duration (e.g., N. Smith et al. 2010; O. D. Fox et al. 2015). We can estimate the progenitor mass-loss rate by assuming $\dot{M} = 4\pi v_{\rm w} \rho_{\rm CSM} R_{\rm CSM}^2$ with a wind velocity $v_{\rm w} = 10$–100 km s^{-1}. This gives a mass-loss rate of 0.1–0.8 $M_\odot$ yr^{-1} for CSM density parameter $s = 2$, which is comparable to that

of SN 2006gy ($0.1\,M_{\odot}\,\mathrm{yr}^{-1}$; E. O. Ofek et al. 2007) and the extreme value inferred for SN-IIn events like iPTF13z, which showed $\dot{M} \sim 0.1$–$2\,M_{\odot}\,\mathrm{yr}^{-1}$ (A. Nyholm et al. 2017). This estimated mass-loss rate is consistent with extreme eruptive episodes such as those seen in luminous blue variables (LBVs) undergoing giant eruptions (see, e.g., N. Smith & S. P. Owocki 2006), or the violent mass ejections predicted by pulsational pair-instability events in very massive stars (S. E. Woosley 2017). This supports the idea that SN 2021aaev's progenitor may have undergone similarly eruptive presupernova mass loss.

7.2. Can SN 2021aaev Be a SN Ia-CSM?

While CSM interaction dominates the observed emission of SN 2021aaev, it also obscures the nature of the underlying explosion. Moreover, the transient location's visual alignment with a low-SFR region ($0.02\,M_{\odot}\,\mathrm{yr}^{-1}$) raises the possibility of an origin other than massive star core collapse. Here, we discuss whether SN 2021aaev could be a Type Ia SN (SN Ia) interacting with CSM (SN Ia-CSM), i.e., a thermonuclear explosion embedded in a dense CSM envelope.

SNe Ia-CSM can sometimes be disguised as SNe IIn or SLSNe-IIn (G. Leloudas et al. 2015), since SN Ia-CSM can reach comparable peak luminosities (as bright as −21.3 mag in the R band; J. M. Silverman et al. 2013) and show prominent Hα. Systematic sample studies (J. M. Silverman et al. 2013; Y. Sharma et al. 2023) have shown that the spectra of less luminous SNe Ia-CSM typically exhibit "diluted" SN Ia features blended with H emission lines, with a Balmer decrement of 5–7. Although such features are not observed in the early-time spectra of SN 2021aaev, it is worth noting, as G. Leloudas et al. (2015) pointed out, that in more luminous cases (<-20.5 mag) the underlying SN Ia features can remain hidden until late phases, especially in cases where $M_{\mathrm{CSM}} \gg M_{\mathrm{ej}}$. In the absence of late-time spectra, we cannot completely rule out the SN Ia-CSM scenario based on current observations.

Notably, A. Jerkstrand et al. (2020) suggested that SN 2006gy, previously considered as a SLSN-IIn, could be explained by a SN Ia-CSM model based on its high inferred nickel mass ($0.5\,M_{\odot}$) and intermediate-width Fe lines in the +394 days spectrum. Despite spectroscopic differences, SN 2021aaev shares several similarities with SN 2006gy. First, they exhibit comparable peak luminosities, total radiated energies, and light-curve timescales. Second, from our simple analytical modeling in Section 5, we inferred an ejecta mass of 1–$2\,M_{\odot}$ that does not rule out a thermonuclear origin, and a CSM mass of $\sim 13\,M_{\odot}$ that matches the CSM estimates for SN 2006gy in A. Jerkstrand et al. (2020). As A. Jerkstrand et al. (2020) proposed, one plausible progenitor scenario capable of producing such a large CSM mass is the inspiral of a white dwarf (WD) into a massive companion with a nondegenerate He core, which can potentially unbind a substantial fraction of the stellar envelope during the process (simulated with a neutron star; similar dynamics are expected for a WD; J. L. Terman et al. 1995).

7.3. Can SN 2021aaev Be a Nuclear Transient?

If we interpret the red clump in Figure 1 with which SN 2021aaev visually aligns as a distinct galaxy, likely a dwarf galaxy interacting with a larger spiral, then we should also consider the possibility that SN 2021aaev is of nuclear origin. One class of nuclear transients is tidal disruption events (TDEs), which can be contaminants in SLSN-II samples (see, e.g., P. J. Pessi et al. 2025b) due to their similarly extreme luminosities and energetics. This is especially relevant in light of recent studies on AT 2022wtn (F. Onori et al. 2025), where a TDE was discovered in an interacting galaxy environment, and AT 2020yue, which was initially considered to be a SLSN-II (T. Kangas et al. 2022) but later reclassified as a TDE by Y. Yao et al. (2023). However, despite the similar location, SN 2021aaev shows photometric and spectroscopic properties that are distinct from those of TDEs. TDEs typically exhibit little color evolution and maintain a constant or even rising blackbody temperature over time (T. Hung et al. 2017; S. van Velzen et al. 2021), whereas SN 2021aaev evolves from blue to red and cools after its peak, behavior more consistent with that of a SN. The spectra of SN 2021aaev evolve on a timescale of tens of days, while TDEs typically show much slower spectral evolution, often remaining blue and only weakly evolving for several months (S. Gezari 2021; S. van Velzen et al. 2021). Hence, we conclude that the observations of SN 2021aaev agree better with an interacting SN interpretation rather than a TDE.

Is it possible that SN 2021aaev is a changing-look active galactic nucleus (CLAGN)? CLAGNs are a subclass of AGNs that change types due to either changes in accretion rate or obscuration (see, e.g., C. Ricci & B. Trakhtenbrot 2023). Owing to their diverse observable properties, some CLAGNs can mimic SLSNe-IIn. A notable example is AT 2022rze (P. J. Pessi et al. 2025a), which is an ambiguously classified transient found in a merging system. However, SN 2021aaev shows smooth, well-behaved photometric and spectroscopic evolution, while CLAGN variability is generally stochastic and persistent. Many CLAGNs display a "turn-on" of broad, persistent Balmer emission that may arise from changes to the accretion state (L. Zhu et al. 2024), and show typical AGN lines such as [O III] $\lambda\lambda$4959,5007, [N II] $\lambda\lambda$6548,6583, and [S II] $\lambda\lambda$6716,6732 (J. M. M. Neustadt et al. 2023). None of these is observed in the case of SN 2021aaev. Therefore, SN 2021aaev is better interpreted as an interacting SN rather than a CLAGN.

8. Conclusion

In this work, we have presented and analyzed a large photometric and spectroscopic dataset of SN 2021aaev, a H-rich, superluminous, interacting SN discovered by ZTF and classified as a SLSN-IIn. Our main conclusions are as follows:

1. SN 2021aaev lies at the luminous (o-band peak at −21.35 mag), fast-evolving ($t_{\mathrm{rise}} = 28.1$ days) side of the SLSN-II population, and has a total radiated energy of 1.41×10^{51} erg.
2. SN 2021aaev shows persistent narrow Balmer lines for ∼100 days, likely explained by continued CSM interaction.
3. Early spectra reveal a fading feature at ∼4650 Å that we identify as a blend of flash-ionized He II, C III, and/or N III lines from dense, confined CSM, making this the first known SLSN-IIn flasher.
4. Analytical modeling favors a scenario in which SN 2021aaev is powered by massive, extensive H-rich CSM ($M_{\mathrm{CSM}} \sim 9$–$19\,M_{\odot}$, $R_{\mathrm{CSM}} \sim 1.3$–$2.0 \times 10^{16}$ cm)

that exceeds the ejecta mass ($M_{\rm ej} \sim 1$–$2\,M_{\odot}$), likely originating from eruptive LBV or pulsational pair-instability episodes. Alternatively, as the massive CSM obscures the true nature of the explosion, a Type Ia-CSM origin cannot be ruled out.

5. SN 2021aaev is visually located on a red substructure (likely a dwarf satellite or a merging companion) within a larger spiral host. The substructure's SED and absence of strong emission lines indicate a quiescent environment (SFR $= 0.02^{+0.13}_{-0.02}\,M_{\odot}\,{\rm yr}^{-1}$).

Overall, SN 2021aaev highlights the challenges in disentangling the underlying explosion mechanisms of SLSNe-IIn from strong CSM interaction. Its combination of early-time flash features, massive CSM, and unusual host environment adds to the observed diversity among H-rich SLSNe.

Acknowledgments

We thank Daniel A. Perley for the observation made with the IO:O instrument on the Liverpool Telescope (LT), and K-Ryan Hinds for the reduction on the photometry taken with the LT. We thank Luc Dessart, Claes Fransson, and Nikhil Sarin for useful discussions. T.-W.C. acknowledges the financial support from the Yushan Fellow Program by the Ministry of Education, Taiwan (grant No. MOE-111-YSFMS-0008-001-P1) and the National Science and Technology Council, Taiwan (NSTC, grant No. 114-2112-M-008-021-MY3). M.N. is supported by the European Research Council (ERC) under the European Union's Horizon 2020 research and innovation program (grant agreement No. 948381). The Oskar Klein Centre is funded by the Swedish Research Council. This project is funded by the European Union (ERC, project number 101042299, TransPIre). Views and opinions expressed are however those of the author(s) only and do not necessarily reflect those of the European Union or the European Research Council Executive Agency. Neither the European Union nor the granting authority can be held responsible for them. Based on observations obtained with the Samuel Oschin Telescope 48 inch and the 60 inch Telescope at the Palomar Observatory as part of the Zwicky Transient Facility (ZTF) project. ZTF is supported by the National Science Foundation under grant Nos. AST-1440341 and AST-2034437, and currently Award No. 2407588. ZTF receives additional funding from the ZTF partnership. Current members include Caltech, USA; Caltech/IPAC, USA; University of Maryland, USA; University of California, Berkeley, USA; University of Wisconsin at Milwaukee, USA; Cornell University, USA; Drexel University, USA; University of North Carolina at Chapel Hill, USA; Institute of Science and Technology, Austria; National Central University, Taiwan; and OKC, University of Stockholm, Sweden. Operations are conducted by Caltech's Optical Observatory (COO), Caltech/IPAC, and the University of Washington at Seattle, USA. SED Machine is based upon work supported by the National Science Foundation under grant No. 1106171. Based on observations collected at the European Southern Observatory under ESO program IDs 106.216C and 108.220C (PI: Inserra). This work has made use of data from ALFOSC, which is provided by the Instituto de Astrofisica de Andalucia (IAA) under a joint agreement with the University of Copenhagen and NOT. The ZTF forced-photometry service was funded under the Heising-Simons Foundation grant No. 12540303 (PI: Graham). This work has made use of data from the Asteroid Terrestrial-impact Last Alert System (ATLAS) project. ATLAS is primarily funded to search for near-Earth asteroids through NASA grant Nos. NN12AR55G, 80NSSC18K0284, and 80NSSC18K1575; byproducts of the NEO search include images and catalogs from the survey area. The ATLAS science products have been made possible through the contributions of the University of Hawaii Institute for Astronomy, Queen's University Belfast, the Space Telescope Science Institute, and the South African Astronomical Observatory. The Liverpool Telescope is operated on the island of La Palma by Liverpool John Moores University in the Spanish Observatorio del Roque de los Muchachos of the Instituto de Astrofisica de Canarias with financial support from the UK Science and Technology Facilities Council.

Facilities: PO:1.2m, PO:1.5m, KAIT, Liverpool:2m, ATLAS, Swift (UVOT), VLT:Kueyen, NOT, NTT.

Software: NUMPY (S. van der Walt et al. 2011), SCIPY (P. Virtanen et al. 2020), MATPLOTLIB (J. D. Hunter 2007), ASTROPY (Astropy Collaboration et al. 2013, 2018), GEORGE (D. Foreman-Mackey 2015), REDBACK (N. Sarin et al. 2024), EMCEE (D. Foreman-Mackey et al. 2013), BAGPIPES (A. C. Carnall et al. 2018), PYSERSIC (I. Pasha & T. B. Miller 2023), Fritz SkyPortal Marshal (S. J. van der Walt et al. 2019; M. W. Coughlin et al. 2023).

Appendix A
Photometric Data for SN 2021aaev

Appendix A provides Table 3, which shows the complete photometric dataset of SN 2021aaev used in this study.

Table 3
Photometric Observations of SN 2021aaev

MJD	Phase[a] (days)	Filter	Magnitude (mag)	Instrument
59486.43	−27.32	*o*	20.595 ± 0.269	ATLAS
59488.33	−25.67	*r*	20.105 ± 0.112	ZTF
59488.38	−25.63	*g*	19.629 ± 0.070	ZTF
59488.51	−25.52	*o*	19.868 ± 0.182	ATLAS
59489.30	−24.83	*i*	19.592 ± 0.146	ZTF
59490.51	−23.79	*o*	19.520 ± 0.116	ATLAS
59492.42	−22.13	*o*	19.559 ± 0.211	ATLAS
59493.44	−21.25	*o*	19.216 ± 0.086	ATLAS
59494.44	−20.39	*o*	18.842 ± 0.066	ATLAS
59496.34	−18.74	*i*	18.772 ± 0.067	ZTF
59496.42	−18.67	*o*	18.558 ± 0.062	ATLAS
59497.43	−17.80	*r*	18.520 ± 0.043	ZTF
59498.15	−17.17	*r*	18.441 ± 0.071	ZTF
59498.47	−16.90	*o*	18.480 ± 0.046	ATLAS
59499.67	−15.86	*V*	18.452 ± 0.193	Swift/UVOT
59499.67	−15.86	UVW2	19.313 ± 0.087	Swift/UVOT
59499.67	−15.86	UVW1	18.940 ± 0.089	Swift/UVOT
59499.67	−15.86	*B*	18.555 ± 0.114	Swift/UVOT
59499.67	−15.86	*U*	18.432 ± 0.084	Swift/UVOT
59499.68	−15.86	UVM2	19.026 ± 0.091	Swift/UVOT
59500.38	−15.25	*o*	18.322 ± 0.059	ATLAS
59501.40	−14.36	*g*	17.890 ± 0.018	ZTF
59501.40	−14.36	*o*	18.321 ± 0.048	ATLAS
59503.21	−12.80	*i*	18.449 ± 0.064	ZTF

Table 3
(Continued)

MJD	Phase[a] (days)	Filter	Magnitude (mag)	Instrument
59503.30	−12.72	*r*	18.151 ± 0.039	ZTF
59503.32	−12.70	*o*	18.383 ± 0.180	ATLAS
59503.34	−12.68	*g*	17.966 ± 0.036	ZTF
59503.35	−12.68	*r*	18.225 ± 0.046	ZTF
59503.39	−12.64	*r*	18.139 ± 0.027	ZTF
59503.39	−12.64	*i*	18.230 ± 0.036	ZTF
59503.39	−12.64	*g*	17.925 ± 0.047	ZTF
59505.21	−11.07	*g*	17.854 ± 0.048	ZTF
59505.29	−10.99	*r*	18.028 ± 0.042	ZTF
59509.22	−7.60	*r*	17.949 ± 0.033	ZTF
59509.25	−7.57	*g*	17.931 ± 0.068	ZTF
59509.25	−7.57	*r*	17.988 ± 0.053	ZTF
59509.26	−7.57	*i*	18.075 ± 0.023	ZTF
59509.32	−7.51	UVW1	17.988 ± 0.079	Swift/UVOT
59509.33	−7.50	*U*	17.847 ± 0.096	Swift/UVOT
59509.33	−7.50	UVM2	18.248 ± 0.073	Swift/UVOT
59509.33	−7.50	*V*	17.727 ± 0.190	Swift/UVOT
59509.33	−7.50	UVW2	18.526 ± 0.087	Swift/UVOT
59509.33	−7.50	*B*	17.682 ± 0.108	Swift/UVOT
59510.42	−6.56	*o*	18.004 ± 0.047	ATLAS
59512.25	−4.97	*i*	18.030 ± 0.032	ZTF
59512.43	−4.82	*o*	18.044 ± 0.047	ATLAS
59514.19	−3.29	*i*	18.001 ± 0.058	ZTF
59514.19	−3.30	*r*	17.973 ± 0.032	ZTF
59514.34	−3.17	*B*	17.709 ± 0.088	Swift/UVOT
59514.34	−3.16	UVW2	18.869 ± 0.083	Swift/UVOT
59514.34	−3.17	*U*	17.776 ± 0.078	Swift/UVOT
59514.34	−3.17	UVW1	18.314 ± 0.074	Swift/UVOT
59514.34	−3.16	*V*	17.368 ± 0.123	Swift/UVOT
59514.35	−3.16	UVM2	18.603 ± 0.069	Swift/UVOT
59516.41	−1.38	*r*	18.076 ± 0.100	ZTF
59516.41	−1.38	*i*	18.090 ± 0.104	ZTF
59516.41	−1.38	*o*	18.074 ± 0.035	ATLAS
59517.27	−0.63	*r*	17.884 ± 0.017	ZTF
59518.40	0.35	*c*	17.921 ± 0.025	ATLAS
59518.75	0.65	UVW1	18.462 ± 0.081	Swift/UVOT
59518.76	0.66	UVW2	18.972 ± 0.088	Swift/UVOT
59518.76	0.65	*U*	17.888 ± 0.085	Swift/UVOT
59518.76	0.66	*V*	17.759 ± 0.163	Swift/UVOT
59518.76	0.66	UVM2	18.831 ± 0.077	Swift/UVOT
59518.76	0.65	*B*	17.651 ± 0.091	Swift/UVOT
59520.27	1.96	*r*	17.927 ± 0.019	ZTF
59520.29	1.98	*g*	17.858 ± 0.017	ZTF
59520.41	2.09	*o*	17.978 ± 0.031	ATLAS
59522.27	3.69	*g*	17.874 ± 0.017	ZTF
59522.28	3.70	*i*	18.014 ± 0.025	ZTF
59522.30	3.72	*r*	17.910 ± 0.017	ZTF
59522.40	3.81	*c*	17.919 ± 0.027	ATLAS
59522.67	4.04	*B*	17.809 ± 0.100	Swift/UVOT
59522.67	4.04	UVW1	18.662 ± 0.087	Swift/UVOT
59522.67	4.04	*U*	18.233 ± 0.098	Swift/UVOT
59522.67	4.04	UVW2	19.161 ± 0.093	Swift/UVOT
59522.68	4.05	UVM2	19.066 ± 0.082	Swift/UVOT
59522.68	4.05	*V*	17.481 ± 0.140	Swift/UVOT
59523.39	4.66	*r*	17.953 ± 0.085	ZTF
59524.15	5.32	*r*	17.984 ± 0.021	ZTF
59524.18	5.35	*r*	17.917 ± 0.017	ZTF
59524.18	5.35	*i*	18.015 ± 0.022	ZTF
59524.18	5.35	*g*	17.989 ± 0.034	ZTF
59524.25	5.41	*r*	17.886 ± 0.018	ZTF
59524.32	5.47	*g*	17.824 ± 0.015	ZTF
59524.34	5.49	*o*	18.087 ± 0.040	ATLAS

Table 3
(Continued)

MJD	Phase[a] (days)	Filter	Magnitude (mag)	Instrument
59525.18	6.21	*i*	18.069 ± 0.036	ZTF
59526.25	7.14	UVW2	19.481 ± 0.100	Swift/UVOT
59526.25	7.14	*r*	17.892 ± 0.017	ZTF
59526.25	7.13	UVW1	18.817 ± 0.090	Swift/UVOT
59526.25	7.14	*U*	18.005 ± 0.087	Swift/UVOT
59526.25	7.14	*V*	17.672 ± 0.158	Swift/UVOT
59526.25	7.14	*B*	17.802 ± 0.096	Swift/UVOT
59526.32	7.20	UVM2	19.293 ± 0.135	Swift/UVOT
59526.32	7.20	*g*	17.885 ± 0.017	ZTF
59526.38	7.25	*c*	17.974 ± 0.024	ATLAS
59528.40	9.00	*o*	18.297 ± 0.063	ATLAS
59529.27	9.76	*i*	18.063 ± 0.037	ZTF
59529.27	9.75	*g*	18.013 ± 0.022	ZTF
59529.34	9.81	*r*	18.009 ± 0.026	ZTF
59530.36	10.69	*r*	18.268 ± 0.105	ZTF
59530.36	10.69	*o*	18.178 ± 0.121	ATLAS
59530.36	10.69	*i*	18.207 ± 0.114	ZTF
59531.24	11.46	*r*	17.972 ± 0.028	ZTF
59531.33	11.54	*g*	18.006 ± 0.029	ZTF
59531.36	11.56	*r*	18.030 ± 0.093	ZTF
59531.36	11.56	*i*	18.009 ± 0.089	ZTF
59532.15	12.24	*i*	18.046 ± 0.041	ZTF
59532.28	12.36	*o*	18.097 ± 0.071	ATLAS
59536.31	15.84	*g*	18.027 ± 0.059	ZTF
59538.20	17.48	*g*	18.015 ± 0.042	ZTF
59538.25	17.53	*r*	17.960 ± 0.029	ZTF
59538.44	17.69	*o*	18.265 ± 0.080	ATLAS
59539.72	18.79	*U*	18.706 ± 0.096	Swift/UVOT
59539.72	18.79	*B*	18.026 ± 0.088	Swift/UVOT
59539.72	18.79	UVW1	19.453 ± 0.095	Swift/UVOT
59539.72	18.79	UVW2	20.083 ± 0.103	Swift/UVOT
59539.72	18.80	*V*	17.803 ± 0.131	Swift/UVOT
59539.73	18.80	UVM2	19.901 ± 0.090	Swift/UVOT
59540.28	19.28	*i*	18.294 ± 0.073	ZTF
59542.18	20.92	*r*	18.053 ± 0.024	ZTF
59542.28	21.01	*g*	18.209 ± 0.043	ZTF
59542.33	21.05	*o*	18.197 ± 0.044	ATLAS
59544.37	22.82	*o*	18.175 ± 0.045	ATLAS
59544.50	22.93	*B*	18.220 ± 0.121	Swift/UVOT
59544.50	22.93	UVW1	19.769 ± 0.134	Swift/UVOT
59544.50	22.93	*U*	18.993 ± 0.137	Swift/UVOT
59544.51	22.94	*V*	18.071 ± 0.195	Swift/UVOT
59544.51	22.94	UVM2	20.131 ± 0.119	Swift/UVOT
59544.51	22.93	UVW2	20.367 ± 0.138	Swift/UVOT
59546.31	24.49	*i*	18.054 ± 0.077	ZTF
59546.31	24.49	*r*	18.034 ± 0.128	ZTF
59546.37	24.55	*o*	18.164 ± 0.037	ATLAS
59547.33	25.37	*i*	18.225 ± 0.121	ZTF
59548.32	26.24	*r*	18.060 ± 0.070	ZTF
59549.51	27.27	UVW1	20.082 ± 0.124	Swift/UVOT
59549.51	27.27	*B*	18.432 ± 0.108	Swift/UVOT
59549.51	27.27	UVW2	20.550 ± 0.121	Swift/UVOT
59549.51	27.27	*U*	18.879 ± 0.104	Swift/UVOT
59549.52	27.27	UVM2	20.279 ± 0.101	Swift/UVOT
59549.52	27.27	*V*	18.060 ± 0.152	Swift/UVOT
59550.32	27.96	*r*	18.335 ± 0.138	ZTF
59550.32	27.97	*i*	18.454 ± 0.112	ZTF
59551.31	28.83	*r*	18.206 ± 0.094	ZTF
59551.32	28.83	*i*	18.291 ± 0.102	ZTF
59553.93	31.09	UVW2	20.753 ± 0.132	Swift/UVOT
59553.93	31.09	*U*	19.278 ± 0.126	Swift/UVOT
59553.93	31.09	*B*	18.509 ± 0.114	Swift/UVOT

Table 3
(Continued)

MJD	Phase[a] (days)	Filter	Magnitude (mag)	Instrument
59553.93	31.09	UVM2	20.699 ± 0.123	Swift/UVOT
59553.93	31.09	*V*	18.160 ± 0.164	Swift/UVOT
59553.93	31.09	UVW1	20.239 ± 0.135	Swift/UVOT
59555.19	32.18	*g*	18.651 ± 0.032	ZTF
59555.20	32.19	*i*	18.433 ± 0.125	ZTF
59555.20	32.19	*r*	18.354 ± 0.045	ZTF
59564.21	39.99	*i*	18.309 ± 0.034	ZTF
59564.21	39.98	*g*	18.985 ± 0.051	ZTF
59564.21	39.98	*r*	18.561 ± 0.036	ZTF
59576.96	51.02	*U*	19.806 ± 0.106	Swift/UVOT
59581.40	54.86	*U*	20.269 ± 0.103	Swift/UVOT
59581.82	55.22	*o*	18.809 ± 0.075	ATLAS
59582.21	55.56	*r*	19.033 ± 0.081	ZTF
59582.21	55.56	*g*	19.635 ± 0.044	ZTF
59582.22	55.56	*i*	18.749 ± 0.032	ZTF
59582.22	55.57	*g*	19.556 ± 0.072	ZTF
59582.22	55.57	*r*	19.099 ± 0.607	ZTF
59582.23	55.57	*i*	18.688 ± 0.035	ZTF
59582.81	56.08	*o*	18.758 ± 0.168	ATLAS
59584.27	57.34	*o*	18.947 ± 0.081	ATLAS
59586.24	59.04	*U*	19.989 ± 0.101	Swift/UVOT
59586.26	59.06	*o*	18.959 ± 0.069	ATLAS
59590.25	62.52	*o*	19.096 ± 0.201	ATLAS
59591.75	63.81	*U*	20.150 ± 0.101	Swift/UVOT
59592.29	64.28	*o*	19.202 ± 0.165	ATLAS
59596.25	67.71	*o*	19.299 ± 0.180	ATLAS
59598.81	69.92	*o*	19.002 ± 0.147	ATLAS
59600.27	71.19	*o*	19.237 ± 0.133	ATLAS
59604.23	74.61	*o*	19.231 ± 0.110	ATLAS
59627.13	94.43	*r*	19.800 ± 0.147	ZTF
59628.12	95.29	*r*	19.659 ± 0.083	ZTF
59629.12	96.15	*r*	19.648 ± 0.085	ZTF
59630.12	97.02	*r*	19.752 ± 0.092	ZTF
59639.12	104.80	*r*	19.506 ± 0.181	ZTF
59640.12	105.67	*r*	19.842 ± 0.173	ZTF
59777.07	224.17	*o*	19.446 ± 0.309	ATLAS

Table 3
(Continued)

MJD	Phase[a] (days)	Filter	Magnitude (mag)	Instrument
59784.13	230.28	*r*	21.385 ± 0.231	ZTF
59784.13	230.27	*i*	20.491 ± 0.167	ZTF
59786.60	232.41	*o*	20.332 ± 0.228	ATLAS
59787.47	233.16	*i*	20.338 ± 0.190	ZTF
59788.44	234.00	*r*	21.274 ± 0.304	ZTF
59791.39	236.56	*c*	21.061 ± 0.312	ATLAS
59794.43	239.19	*i*	20.380 ± 0.248	ZTF
59795.10	239.77	*g*	21.398 ± 0.223	ZTF
59795.10	239.77	*r*	21.496 ± 0.271	ZTF
59795.10	239.77	*i*	20.746 ± 0.199	ZTF
59796.48	240.96	*g*	21.489 ± 0.287	ZTF
59809.42	252.16	*g*	20.745 ± 0.282	ZTF
59809.44	252.18	*i*	20.480 ± 0.240	ZTF
59809.47	252.20	*r*	20.813 ± 0.275	ZTF
59810.53	253.12	*o*	20.244 ± 0.275	ATLAS
59812.41	254.74	*r*	21.236 ± 0.259	ZTF
59813.04	255.29	*o*	20.508 ± 0.250	ATLAS
59815.40	257.33	*i*	20.486 ± 0.196	ZTF
59816.46	258.25	*r*	21.254 ± 0.288	ZTF
59816.46	258.25	*g*	21.290 ± 0.242	ZTF
59827.40	267.72	*i*	20.665 ± 0.255	ZTF
59828.45	268.63	*r*	21.300 ± 0.289	ZTF
59841.40	279.83	*g*	21.802 ± 0.298	ZTF
59846.34	284.10	*i*	20.421 ± 0.224	ZTF
59848.35	285.84	*r*	21.279 ± 0.274	ZTF
59850.34	287.56	*r*	21.281 ± 0.247	ZTF
59857.36	293.64	*i*	20.458 ± 0.273	ZTF
59872.47	306.71	*c*	20.573 ± 0.234	ATLAS
59883.28	316.06	*i*	20.741 ± 0.288	ZTF
59894.37	325.66	*o*	20.312 ± 0.298	ATLAS
59895.25	326.43	*i*	20.546 ± 0.300	ZTF

Note.
[a] Rest-frame days since ATLAS *o*-band peak on MJD 59518.0.

(This table is available in its entirety in machine-readable form in the online article.)

Appendix B
Spectroscopic Data for SN 2021aaev

Appendix B provides Table 4 which shows the complete spectroscopic dataset for SN 2021aaev used in this study.

Table 4
Spectroscopic Observations of SN 2021aaev

UT	MJD	Phase[a] (days)	Telescope +Instrument	Exposure (s)	Grism(s), Slit	Wavelength Range (Å)
2021-10-10	59497.96	−17.35	LT+SPRAT	600	⋯	4000–8000
2021-10-11	59498.15	−17.18	SEDM+P60	2700	⋯	3800–9200
2021-10-12	59499.17	−16.29	NOT+ALFOSC	1800	Gr#4, 1.″3	3500–9600
2021-10-14	59501.29	−14.46	VLT+X-Shooter	1200/1229/300	Gr#4, 1.″3	3000–24800
2021-10-16	59503.33	−12.59	NTT+EFOSC2	600	Gr#13, 1.″0	3650–9250
2021-10-16	59503.34	−12.68	SEDM+P60	2700	⋯	3800–9200
2021-10-22	59509.22	−7.60	SEDM+P60	2700	⋯	3800–9200
2021-10-26	59513.10	−4.24	NTT+EFOSC2	1800*2+1800	Gr#11+Gr#16, 1.″0	3350–10000
2021-11-06	59498.15	5.32	SEDM+P60	2160	⋯	3800–9200
2021-11-27	59545.19	23.53	NTT+EFOSC2	1800*2	Gr#11, 1.″0	3350–7470
2021-12-03	59551.17	28.71	NTT+EFOSC2	1800*2	Gr#16, 1.″0	6000–10000
2021-12-22	59570.91	45.78	NOT+ALFOSC	3600	Gr#4, 1.″0	3500–9600
2022-01-03	59582.09	55.47	NTT+EFOSC2	2700+2700	Gr#11+Gr#16, 1.″0	3350–10000

Note.
[a] Rest-frame days since ATLAS *o*-band peak on MJD 59518.0.

(This table is available in its entirety in machine-readable form in the online article.)

Appendix C
Result from Analytical CSM-interaction Models

Appendix C provides Figures 25 and 26, which show fitted parameters of the analytical CSM-interaction modeling performed in this study.

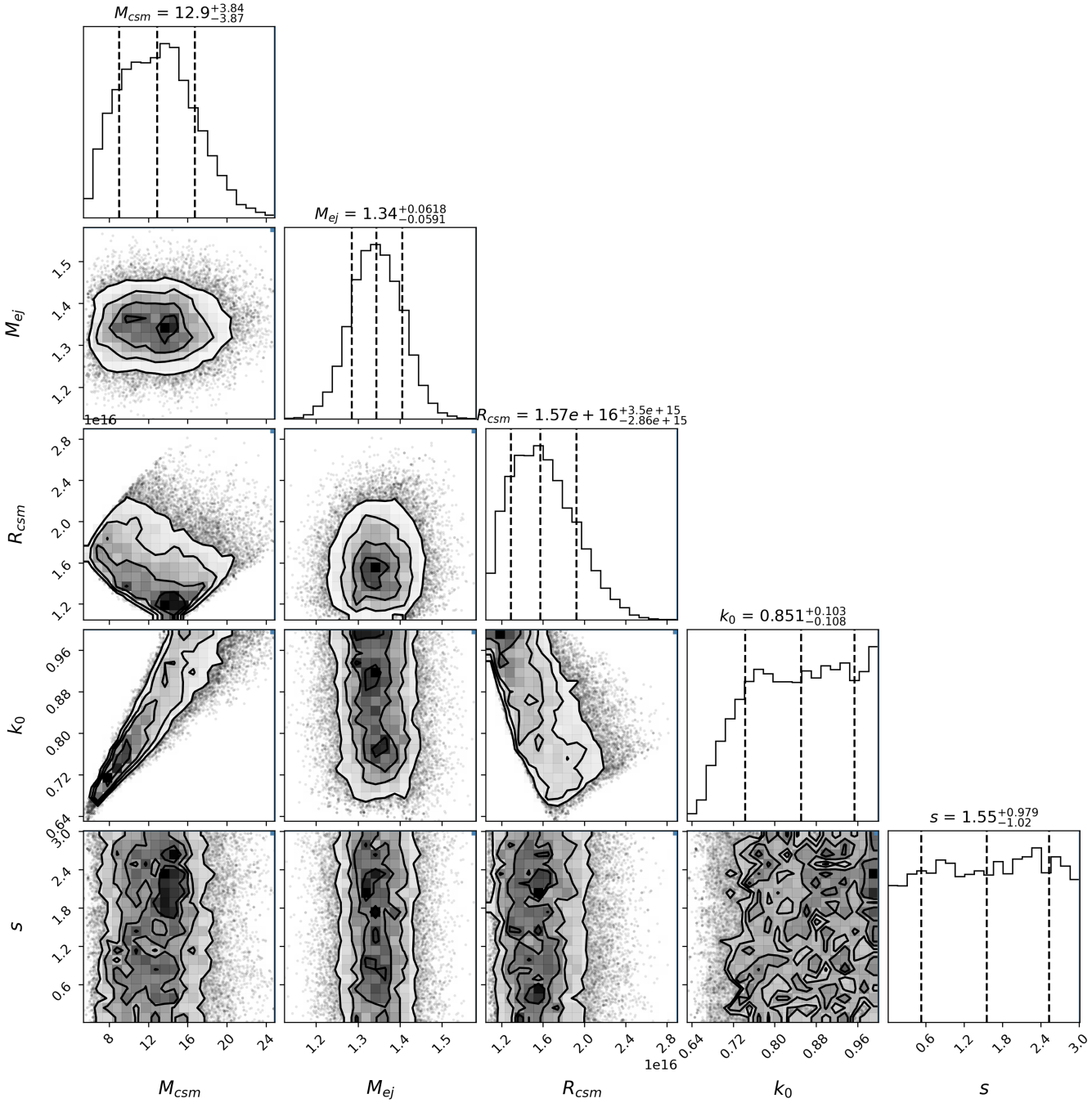

Figure 25. Corner plot of fitted parameters of SN 2021aaev using the interior breakout CSM-interaction analytical model (D. K. Khatami & D. N. Kasen 2024), showing their median values and 1σ spreads. The sample was drawn using `emcee`.

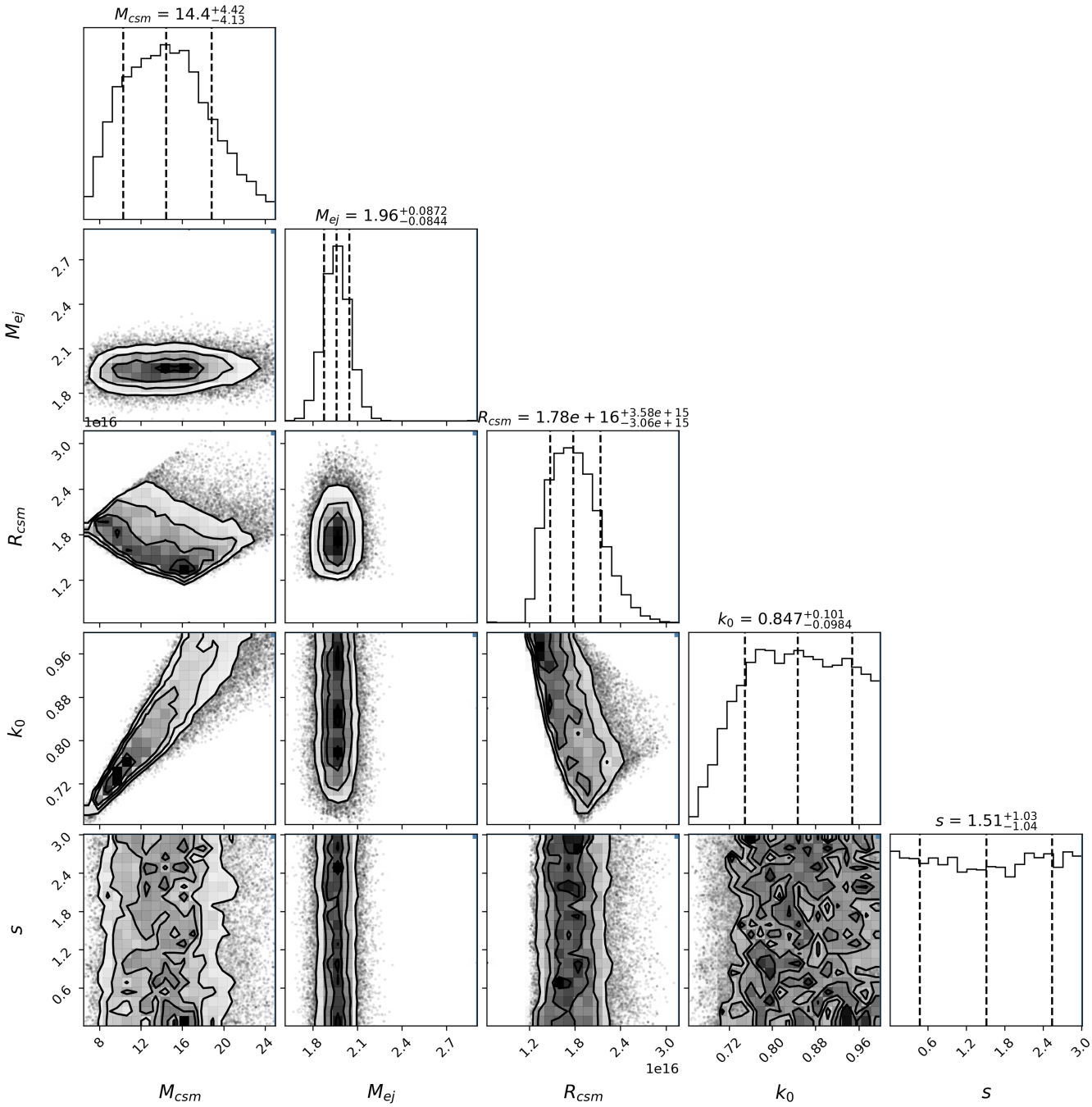

Figure 26. Corner plot of fitted parameters of SN 2021aaev using the interior breakout CSM-interaction analytical model (D. K. Khatami & D. N. Kasen 2024), showing their median values and 1σ spreads. This has the additional constraint that the energy conversion efficiency is $\epsilon = 0.6$. The sample was drawn using `emcee`.

ORCID iDs

Yang Hu (胡 阳) https://orcid.org/0000-0002-9744-3910
Ragnhild Lunnan https://orcid.org/0000-0001-9454-4639
Priscila J. Pessi https://orcid.org/0000-0002-8041-8559
Alberto Saldana-Lopez https://orcid.org/0000-0001-8419-3062
Anders Jerkstrand https://orcid.org/0000-0001-8005-4030
Jesper Sollerman https://orcid.org/0000-0003-1546-6615
Steve Schulze https://orcid.org/0000-0001-6797-1889
Joseph P. Anderson https://orcid.org/0000-0003-0227-3451
Seán J. Brennan https://orcid.org/0000-0003-1325-6235
Stefano P. Cosentino https://orcid.org/0000-0001-8082-5296
Anjasha Gangopadhyay https://orcid.org/0000-0002-3884-5637
Anamaria Gkini https://orcid.org/0009-0000-9383-2305
Mariusz Gromadzki https://orcid.org/0000-0002-1650-1518
Matthew J. Hayes https://orcid.org/0000-0001-8587-218X
Cosimo Inserra https://orcid.org/0000-0002-3968-4409
Tomás E. Müller-Bravo https://orcid.org/0000-0003-3939-7167
Matt Nicholl https://orcid.org/0000-0002-2555-3192
Giuliano Pignata https://orcid.org/0000-0003-0006-0188

Avinash Singh https://orcid.org/0000-0003-2091-622X
Jacob L. Wise https://orcid.org/0000-0003-0733-2916
Lin Yan https://orcid.org/0000-0003-1710-9339
Judy Adler https://orcid.org/0009-0006-7265-2747
Ting-Wan Chen https://orcid.org/0000-0002-1066-6098
Tracy X. Chen https://orcid.org/0000-0001-9152-6224
Mansi M. Kasliwal https://orcid.org/0000-0002-5619-4938
Thallis Pessi https://orcid.org/0000-0001-6540-0767
Irene Salmaso https://orcid.org/0000-0003-1450-0869
David R. Young https://orcid.org/0000-0002-1229-2499

References

Astropy Collaboration, Price-Whelan, A. M., Sipőcz, B. M., et al. 2018, AJ, 156, 123
Astropy Collaboration, Robitaille, T. P., Tollerud, E. J., et al. 2013, A&A, 558, A33
Barkat, Z., Rakavy, G., & Sack, N. 1967, PhRvL, 18, 379
Bellm, E. C., Kulkarni, S. R., Graham, M. J., et al. 2019, PASP, 131, 018002
Blagorodnova, N., Neill, J. D., Walters, R., et al. 2018, PASP, 130, 035003
Brennan, S. J., Schulze, S., Lunnan, R., et al. 2024, A&A, 690, A259
Bruch, R. J., Gal-Yam, A., Yaron, O., et al. 2023, ApJ, 952, 119
Bruzual, G., & Charlot, S. 2003, MNRAS, 344, 1000
Calzetti, D., Armus, L., Bohlin, R. C., et al. 2000, ApJ, 533, 682
Carini, R., Gutierrez, C., & Yaron, O. 2021, TNSCR, 2021-3546, 1https://ui.adsabs.harvard.edu/abs/2021TNSCR3546....1C
Carnall, A. C., McLure, R. J., Dunlop, J. S., & Davé, R. 2018, MNRAS, 480, 4379
Chatzopoulos, E., Wheeler, J. C., Vinko, J., Horvath, Z. L., & Nagy, A. 2013, ApJ, 773, 76
Chatzopoulos, E., Wheeler, J. C., Vinko, J., et al. 2011, ApJ, 729, 143
Chen, T.-W. 2019, The Extragalactic Explosive Universe: the New Era of Transient Surveys and Data-Driven Discovery, 15, Zenodo, doi:10.5281/zenodo.3478022
Chen, Z. H., Yan, L., Kangas, T., et al. 2023a, ApJ, 943, 41
Chen, Z. H., Yan, L., Kangas, T., et al. 2023b, ApJ, 943, 42
Chevalier, R. A., & Fransson, C. 1994, ApJ, 420, 268
Chugai, N. N. 1997, Ap&SS, 252, 225
Chugai, N. N., Chevalier, R. A., & Lundqvist, P. 2004, MNRAS, 355, 627
Chugai, N. N., Cumming, R. J., Blinnikov, S. I., et al. 2005, IAUC, 99, 111
Cosentino, S. P., Pumo, M. L., & Cherubini, S. 2025, MNRAS, 540, 2894
Coughlin, M. W., Bloom, J. S., Nir, G., et al. 2023, ApJS, 267, 31
Dekany, R., Smith, R. M., Riddle, R., et al. 2020, PASP, 132, 038001
Dessart, L., Hillier, D. J., & Audit, E. 2017, A&A, 605, A83
Dessart, L., Hillier, D. J., Gezari, S., Basa, S., & Matheson, T. 2009, MNRAS, 394, 21
Dexter, J., & Kasen, D. 2013, ApJ, 772, 30
Fitzpatrick, E. L. 1999, PASP, 111, 63
Foreman-Mackey, D. 2015, George: Gaussian Process regression, Astrophysics Source Code Library, ascl:1511.015
Foreman-Mackey, D., Hogg, D. W., Lang, D., & Goodman, J. 2013, PASP, 125, 306
Fox, O. D., Smith, N., Ammons, S. M., et al. 2015, MNRAS, 454, 4366
Fransson, C., Ergon, M., Challis, P. J., et al. 2014, ApJ, 797, 118
Fremling, C., Sollerman, J., Taddia, F., et al. 2016, A&A, 593, A68
Gal-Yam, A. 2012, Sci, 337, 927
Gal-Yam, A. 2019, ARA&A, 57, 305
Gal-Yam, A., Arcavi, I., Ofek, E. O., et al. 2014, Natur, 509, 471
Gal-Yam, A., Kasliwal, M. M., Arcavi, I., et al. 2011, ApJ, 736, 159
Gehrels, N., Chincarini, G., Giommi, P., et al. 2004, ApJ, 611, 1005
Gezari, S. 2021, ARA&A, 59, 21
Gezari, S., Halpern, J. P., Grupe, D., et al. 2009, ApJ, 690, 1313
Goldoni, P., Royer, F., François, P., et al. 2006, SPIE, 6269, 62692K
Götberg, Y., de Mink, S. E., & Groh, J. H. 2017, A&A, 608, A11
Graham, M. J., Kulkarni, S. R., Bellm, E. C., et al. 2019, PASP, 131, 078001
Gutiérrez, C. P., Pastorello, A., Bersten, M., et al. 2022, MNRAS, 517, 2056
Heger, A., Fryer, C. L., Woosley, S. E., Langer, N., & Hartmann, D. H. 2003, ApJ, 591, 288
Hiramatsu, D., Berger, E., Gomez, S., et al. 2024, arXiv:2411.07287
Hogg, D. W., Baldry, I. K., Blanton, M. R., & Eisenstein, D. J. 2002, arXiv:astro-ph/0210394
Hung, T., Gezari, S., Blagorodnova, N., et al. 2017, ApJ, 842, 29
Hunter, J. D. 2007, CSE, 9, 90
Inserra, C., Smartt, S. J., Gall, E. E. E., et al. 2018, MNRAS, 475, 1046
Janka, H.-T. 2012, ARNPS, 62, 407
Jerkstrand, A., Maeda, K., & Kawabata, K. S. 2020, Sci, 367, 415
Kangas, T., Charalampopoulos, P., Nagao, T., et al. 2026, A&A, 705, A52
Kangas, T., Yan, L., Schulze, S., et al. 2022, MNRAS, 516, 1193
Kankare, E., Ergon, M., Bufano, F., et al. 2012, MNRAS, 424, 855
Kasen, D., & Bildsten, L. 2010, ApJ, 717, 245
Kausch, W., Noll, S., Smette, A., et al. 2015, A&A, 576, A78
Khatami, D. K., & Kasen, D. N. 2024, ApJ, 972, 140
Khazov, D., Yaron, O., Gal-Yam, A., et al. 2016, ApJ, 818, 3
Kim, Y. L., Rigault, M., Neill, J. D., et al. 2022, PASP, 134, 024505
Kroupa, P. 2001, MNRAS, 322, 231
Laplace, E., Götberg, Y., de Mink, S. E., Justham, S., & Farmer, R. 2020, A&A, 637, A6
Leloudas, G., Hsiao, E. Y., Johansson, J., et al. 2015, A&A, 574, A61
Li, W. D. 2000, AIPC, 522, 103
Lucy, L. B., & Solomon, P. M. 1970, ApJ, 159, 879
Masci, F. J., Laher, R. R., Rusholme, B., et al. 2019, PASP, 131, 018003
Masci, F. J., Laher, R. R., Rusholme, B., et al. 2023, arXiv:2305.16279
Matsuoka, T., Maeda, K., & Chen, K.-J. 2025, ApJL, 988, L53
Mazzali, P. A., Sullivan, M., Pian, E., Greiner, J., & Kann, D. A. 2016, MNRAS, 458, 3455
Miller, A. A., Chornock, R., Perley, D. A., et al. 2009, ApJ, 690, 1303
Modigliani, A., Goldoni, P., Royer, F., et al. 2010, SPIE, 7737, 773728
Moran, S., Fraser, M., Kotak, R., et al. 2023, A&A, 669, A51
Moriya, T. J., Nicholl, M., & Guillochon, J. 2018, ApJ, 867, 113
Munoz-Arancibia, A., Forster, F., Bauer, F. E., et al. 2021, TNSTR, 2021-3364, 1https://ui.adsabs.harvard.edu/abs/2021TNSTR3364....1M
Neustadt, J. M. M., Hinkle, J. T., Kochanek, C. S., et al. 2023, MNRAS, 521, 3810
Nicholl, M. 2021, A&G, 62, 5.34
Nicholl, M., Guillochon, J., & Berger, E. 2017, ApJ, 850, 55
Nyholm, A., Sollerman, J., Taddia, F., et al. 2017, A&A, 605, A6
Nyholm, A., Sollerman, J., Tartaglia, L., et al. 2020, A&A, 637, A73
Ofek, E. O., Cameron, P. B., Kasliwal, M. M., et al. 2007, ApJL, 659, L13
Ofek, E. O., Zoglauer, A., Boggs, S. E., et al. 2014, ApJ, 781, 42
Oke, J. B., & Sandage, A. 1968, ApJ, 154, 21
Onori, F., Nicholl, M., Ramsden, P., et al. 2025, MNRAS, 540, 498
Ostriker, J. P., & Gunn, J. E. 1971, ApJL, 164, L95
Pasha, I., & Miller, T. B. 2023, JOSS, 8, 5703
Pearson, J., Hosseinzadeh, G., Sand, D. J., et al. 2023, ApJ, 945, 107
Perley, D. A., Quimby, R. M., Yan, L., et al. 2016, ApJ, 830, 13
Pessi, P. J., Lunnan, R., Sollerman, J., et al. 2025a, MNRAS, 542, 3354
Pessi, P. J., Lunnan, R., Sollerman, J., et al. 2025b, A&A, 695, A142
Petrovic, J., Langer, N., & van der Hucht, K. A. 2005, A&A, 435, 1013
Piascik, A. S., Steele, I. A., Bates, S. D., et al. 2014, SPIE, 9147, 91478H
Planck Collaboration, Aghanim, N., Akrami, Y., et al. 2020, A&A, 641, A1
Poznanski, D., Prochaska, J. X., & Bloom, J. S. 2012, MNRAS, 426, 1465
Puls, J., Vink, J. S., & Najarro, F. 2008, A&ARv, 16, 209
Quimby, R. M., De Cia, A., Gal-Yam, A., et al. 2018, ApJ, 855, 2
Quimby, R. M., Kulkarni, S. R., Kasliwal, M. M., et al. 2011, Natur, 474, 487
Quimby, R. M., Yuan, F., Akerlof, C., & Wheeler, J. C. 2013, MNRAS, 431, 912
Rasmussen, C. E., & Williams, C. K. I. 2005, Gaussian Processes for Machine Learning (MIT Press)
Ricci, C., & Trakhtenbrot, B. 2023, NatAs, 7, 1282
Rigault, M., Neill, J. D., Blagorodnova, N., et al. 2019, A&A, 627, A115
Rodríguez, Ó., Pignata, G., Hamuy, M., et al. 2019, MNRAS, 483, 5459
Roming, P. W. A., Kennedy, T. E., Mason, K. O., et al. 2005, SSRv, 120, 95
Roy, J. R., Arsenault, R., & Joncas, G. 1986, ApJ, 300, 624
Sarin, N., Hubner, M., Omand, C. M. B., et al. 2024, MNRAS, 531, 1203
Schlafly, E. F., & Finkbeiner, D. P. 2011, ApJ, 737, 103
Schlegel, D. J., Finkbeiner, D. P., & Davis, M. 1998, ApJ, 500, 525
Schlegel, E. M. 1990, MNRAS, 244, 269
Schulze, S., Fransson, C., Kozyreva, A., et al. 2024, A&A, 683, A223
Schulze, S., Yaron, O., Sollerman, J., et al. 2021, ApJS, 255, 29
Selsing, J., Malesani, D., Goldoni, P., et al. 2019, A&A, 623, A92
Sharma, Y., Sollerman, J., Fremling, C., et al. 2023, ApJ, 948, 52
Shingles, L., Smith, K. W., Young, D. R., et al. 2021, TNSAN, 7, 1https://ui.adsabs.harvard.edu/abs/2021TNSAN...7....1S
Silverman, J. M., Nugent, P. E., Gal-Yam, A., et al. 2013, ApJS, 207, 3
Smartt, S. J., Valenti, S., Fraser, M., et al. 2015, A&A, 579, A40
Smette, A., Sana, H., Noll, S., et al. 2015, A&A, 576, A77
Smith, K. W., Smartt, S. J., Young, D. R., et al. 2020, PASP, 132, 085002
Smith, N., & Arnett, W. D. 2014, ApJ, 785, 82
Smith, N., Chornock, R., Silverman, J. M., Filippenko, A. V., & Foley, R. J. 2010, ApJ, 709, 856

Smith, N., Li, W., Foley, R. J., et al. 2007, ApJ, 666, 1116
Smith, N., & Owocki, S. P. 2006, ApJL, 645, L45
Sollerman, J., Cumming, R. J., & Lundqvist, P. 1998, ApJ, 493, 933
Soumagnac, M. T., Ofek, E. O., Liang, J., et al. 2020, ApJ, 899, 51
Steele, I. A., Smith, R. J., Rees, P. C., et al. 2004, SPIE, 5489, 679
Stoll, R., Prieto, J. L., Stanek, K. Z., et al. 2011, ApJ, 730, 34
Stone, R. P. S. 1977, ApJ, 218, 767
Suzuki, A., Nicholl, M., Moriya, T. J., & Takiwaki, T. 2021, ApJ, 908, 99
Taylor, M., Cinabro, D., Dilday, B., et al. 2014, ApJ, 792, 135
Terman, J. L., Taam, R. E., & Hernquist, L. 1995, ApJ, 445, 367
Terreran, G., Pumo, M. L., Chen, T.-W., et al. 2017, NatAs, 1, 713
Thornton, I., Villar, V. A., Gomez, S., & Hosseinzadeh, G. 2023, AAS Meeting, 241, 107.24https://ui.adsabs.harvard.edu/abs/2023AAS...24110724T
Tonry, J. L., Denneau, L., Heinze, A. N., et al. 2018, PASP, 130, 064505
van der Walt, S., Colbert, S. C., & Varoquaux, G. 2011, CSE, 13, 22
van der Walt, S. J., Crellin-Quick, A., & Bloom, J. S. 2019, JOSS, 4, 1247
van Dokkum, P. G. 2001, PASP, 113, 1420
van Velzen, S., Gezari, S., Hammerstein, E., et al. 2021, ApJ, 908, 4
Vernet, J., Dekker, H., D'Odorico, S., et al. 2011, A&A, 536, A105
Virtanen, P., Gommers, R., Oliphant, T. E., et al. 2020, NatMe, 17, 261
Woosley, S. E. 2010, ApJL, 719, L204
Woosley, S. E. 2017, ApJ, 836, 244
Woosley, S. E., Blinnikov, S., & Heger, A. 2007, Natur, 450, 390
Woosley, S. E., Heger, A., & Weaver, T. A. 2002, RvMP, 74, 1015
Yang, Y.-P., Liu, X., Pan, Y., et al. 2024, ApJ, 969, 126
Yao, Y., Ravi, V., Gezari, S., et al. 2023, ApJL, 955, L6
Yaron, O., & Gal-Yam, A. 2012, PASP, 124, 668
Yaron, O., Perley, D. A., Gal-Yam, A., et al. 2017, NatPh, 13, 510
Yoon, S.-C., Dessart, L., & Clocchiatti, A. 2017, ApJ, 840, 10
Zhu, L., Li, J., Wang, Z., & Zhang, J. 2024, MNRAS, 530, 3538